Carderock Division, Naval Surface Warfare Center

Bethesda, Maryland 20817-5700

DTNS3D Computer Code Simulation of Tip-Vortex Formation: RANS Code Validation

by
John G. Telste
Roderick M. Coleman
Joseph J. Gorski

19980514 015

DTIC QUALITY INSPECTED 2

REPORT DOCUMENTATION PAGE

1a. REPORT SECURITY CLASSIFICATION UNCLASSIFIED		1b. RESTRICTIVE MARKINGS	
2a. SECURITY CLASSIFICATION AUTHORITY		3 DISTRIBUTION/AVAILABILITY OF REPORT Approved for public release; distribution is unlimited.	
2b. DECLASSIFICATION/DOWNGRADING SCHEDULE			
4. PERFORMING ORGANIZATION REPORT NUMBER(S) NSWCCD-TR-20–97/013		5. MONITORING ORGANIZATION REPORT NUMBER(S)	
6A. NAME OF PERFORMING ORGANIZATION Carderock Division Naval Surface Warfare Center	6b. OFFICE SYMBOL (If applicable) Code 262	7a. NAME OF MONITORING ORGANIZATION	
6c. ADDRESS (City, State, and ZIP Code) Carderock Division Naval Surface Warfare Center Bethesda, MD 20817-5700		7b. ADDRESS (CITY, STATE, AND ZIP CODE)	
8a. NAME OF FUNDING/SPONSORING ORGANIZATION	6b. OFFICE SYMBOL (If applicable)	9. PROCUREMENT INSTRUMENT IDENTIFICATION NUMBER	

8c. ADDRESS (City, State, and ZIP code)	10. SOURCE OF FUNDING NUMBERS			
	PROGRAM ELEMENT NO. PE0602323N	PROJECT NO. RB23H16	TASK NO. 2	WORK UNIT ACCESSION NO. 5060-435

11. TITLE (Include Security Classification)
DTNS3D Computer Code Simulation of Tip-Vortex Formation: RANS Code Validation

12. PERSONAL AUTHOR(S)
Telste, John G., Roderick M. Coleman, and Joseph J. Gorski

13a. TYPE OF REPORT Final	13b. TIME COVERED FROM_____ TO_____	14. DATE OF REPORT (Year, Month, Day) 1997, August	15. PAGE COUNT 54

16. SUPPLEMENTARY NOTATION

17. COSATI CODES			18. SUBJECT TERMS (Continue on Reverse if Necessary and Identify by Block Number)
FIELD	GROUP	SUB-GROUP	Navier-Stokes Equations Vortices Vortex Computations

19. ABSTRACT (Continue on reverse if necessary and identify by block number)

   This report describes results of an effort to simulate the formation of a tip vortex on a wing attached to a half-body and the propagation of the vortex downstrteam from the wing using the Reynolds averaged Navier-Stokes (RANS) computer code DTNS3D. Computational results are presented for the Baldwin-Lomax turbulence model. Three components of the mean velocity in four planes behind the wing are compared with measurements obtained in experiments performed in the MIT water tunnel. The axial component of vorticity is also compared with experimental measurements in the four planes.

20. DISTRIBUTION/AVAILABILITY OF ABSTRACT ☒ UNCLASSIFIED/UNLIMITED ☐ SAME AS RPT. ☐ DTIC USERS	21. ABSTRACT SECURITY CLASSIFICATION UNCLASSIFIED	
22a. NAME OF RESPONSIBLE INDIVIDUAL John G. Telste	22b. TELEPHONE (Include Area Code) (301) 227-1932	22c. OFFICE SYMBOL Code 262

DD FORM 1473, 84 MAR

CONTENTS

FIGURES

TABLES

U.S. CUSTOMARY/METRIC UNITS

1 foot (ft)	=	0.3048 meters (m)
1 inch (in.)	=	25.40 millimeters (mm)
1 foot per second (ft/s)	=	0.3048 meter per second (m/s)
1 degree (angle)	=	0.01745 radians (rad)

ABSTRACT

*This report describes results of an effort to simulate the forma-
tion of a tip vortex on a wing attached to a half-body and the propaga-
tion of the vortex downstream from the wing using the Reynolds averaged
Navier-Stokes (RANS) computer code DTNS3D. Computational results
are presented for the Baldwin-Lomax turbulence model. Three compo-
nents of the mean velocity in four planes behind the wing are compared
with measurements obtained in experiments performed in the MIT water
tunnel. The axial component of vorticity is also compared with experi-
mental measurements in the four planes.*

ADMINISTRATIVE INFORMATION

INTRODUCTION

An accurate numerical prediction of the flow near the tip of a wing is a challenging problem. Po-
tential flow models that make use of a vortex lattice or a dipole sheet can be used to model the flow in the
wake of a wing. The model suffices for applications in which integrated quantities such as the lift are of
interest. However, to accurately compute many of the fine details of the flow such as those associated
with the tip vortex, inclusion of viscous effects is critical. It is important for obtaining a correct predic-
tion of the momentum deficit in the core. The thickness of the viscous-flow boundary layer and where
transition to turbulence occurs within the boundary layer affect the position of the tip vortex core.

Before the appearance of large high-speed computers, alternatives for numerical modeling of tip
vortex generation were limited to the use of potential flow models. The simplest of these is potential flow
supplemented by a trailing horseshoe vortex system. More sophisticated potential flow treatments similar
to those used in MIT's propeller program PSF10 are now possible. Potential flow models assume that the
flow is steady-state and require *a priori* knowledge of the location of an infinitely thin sheet of vorticity
trailing behind the wing. This requirement may be overcome by some sort of iterative technique in which
the position of the wake is adjusted until all the appropriate boundary conditions are satisfied.

Over the last two decades increased computer capabilities have allowed computational fluid dy-
namicists to experiment with the use of simplified Navier-Stokes equations for predicting tip-vortex gen-
eration. In 1979, for example, Shamroth and Briley[1] reported on an effort to apply a viscous-flow com-
putational method to a tip-vortex generation problem. The computational requirements were reduced by
using a marching technique similar to that used by parabolized Navier-Stokes codes. The purpose of their
work was to determine the cause of tip-vortex generation and to present quantitative results for a particu-
lar case. They present contour plots of the streamwise component of vorticity and of velocity in seven
planes perpendicular to the flow. Projections of velocity vectors onto these same planes are also plotted.
All of these planes intersect the wing; in other words, none of them lie in the wake downstream of the
wing. Their computations were performed for a wing of rectangular planform at a 6-deg angle of attack
with 10^6 as the Reynolds number of the flow (based on chord length). The computations showed that, as
in experiments, tip-vortex generation arises from the boundary layer set up in the flow around the tip due

1

to the pressure difference between the lower and upper surfaces of the wing. The thickness of the wing was not taken into account in their computations. In 1985, Govindan *et al.*[2] reported on the calculation of flow near simplified propeller blades. The calculation included computing the tip-vortex generation using parabolized Navier-Stokes equations. No detailed quantitative comparisons of computed results with experimental measurements were made in the paper. More recently, in 1994, Eça *et al.*[3] presented results of their efforts to predict tip-vortex formation. They compute flow near the tip of a wing using partially parabolized Reynolds-averaged Navier-Stokes equations and an algebraic eddy viscosity turbulence model. Numerical results are compared with experimental results. The computed location of the tip-vortex core agreed well with measurement of the core location.

This report describes an attempt to use the full Reynolds-averaged Navier-Stokes equations for the computation of the tip vortex in flow past a simple geometry. The geometry is that of a horizontal wing attached to a vertical half-thickness wing which, in turn, is attached to a wall. Numerical predictions of the three velocity components and the vorticity in four planes downstream of the wing are compared with detailed flow measurements obtained from experiments. The work of this report is the near-field complement to the far-field work described in a recent report by Haussling.[4]

GEOMETRY AND MEASUREMENTS

An experiment was conducted in the MIT Hydrodynamics Laboratory for flow past essentially the same geometric configuration for which calculations are presented in this report.[5]

The geometry of the experiment involves a horizontal wing mounted on a vertical half-thickness wing. The vertical half-thickness wing spans nearly the entire water tunnel which has an almost square cross section of 19.5 in. on each side. It has a chord length of 16 in. and its thickness is half the thickness of a NACA four-digit wing profile with a 22.15 percent thickness ratio. The horizontal wing has a span of 8.06 in., a root chord of 7.5 in., and a tip chord of 4.905 in. The thickness distribution at the root is given by the NACA 0018 wing profile.[6] The tip is rounded and is formed by rotating a NACA 0012 wing profile about the chord. The leading edge has a 9.23-deg sweep angle. The horizontal wing is mounted by means of a shaft at the 1/4-chord position on a pedestal so that it can be rotated through various angles of attack. The pedestal is attached to the vertical half-thickness wing at the half-span position. The shaft through it to the horizontal wing is at the 28 percent chord position of the vertical half-thickness wing. The vertical half-thickness wing is mounted on a plate. The plate, in turn, is mounted on blocks that are attached to the tunnel wall. Figure 1 shows two views of this configuration.

Although the computational geometry is essentially the same as the experimental geometry, simplifications were made to aid in the task of obtaining a computational grid. First, the geometry used in the computations does not include this pedestal. Thus the horizontal wing is mounted directly on the vertical wing. Second, the splitter plates are ignored and the vertical half-thickness wing is mounted directly on the wall. Figure 2 shows a perspective view of the geometry used in the computations. These changes in geometry are near the root of the horizontal wing.

The measurements with which this report is concerned are for a 5.36-deg angle of attack. The free-stream velocity is 26.4 ft/s. Turbulence stimulators are placed at a position 20 percent of the chord behind the leading edge to ensure transition to a turbulent boundary layer at this location on the wing.

Detailed experimental data were collected in four planes perpendicular to the free-stream at distances 9 mm, 70 mm, 136 mm, and 263 mm downstream from the wing tip. The planes have been labeled 1, 1A, 2, and 3, respectively. For the first three planes, data are available from measurements taken on both coarse and fine grids. The coarse grids have a data spacing of 5 mm; the fine grids, a spacing of 0.5 mm. For plane 3, the most downstream of the four planes, data are available only from measure-

(a)

(b)
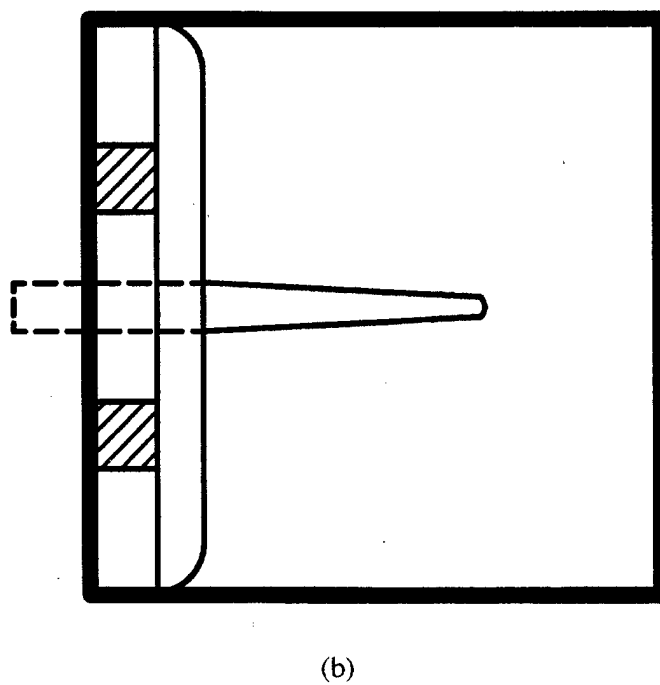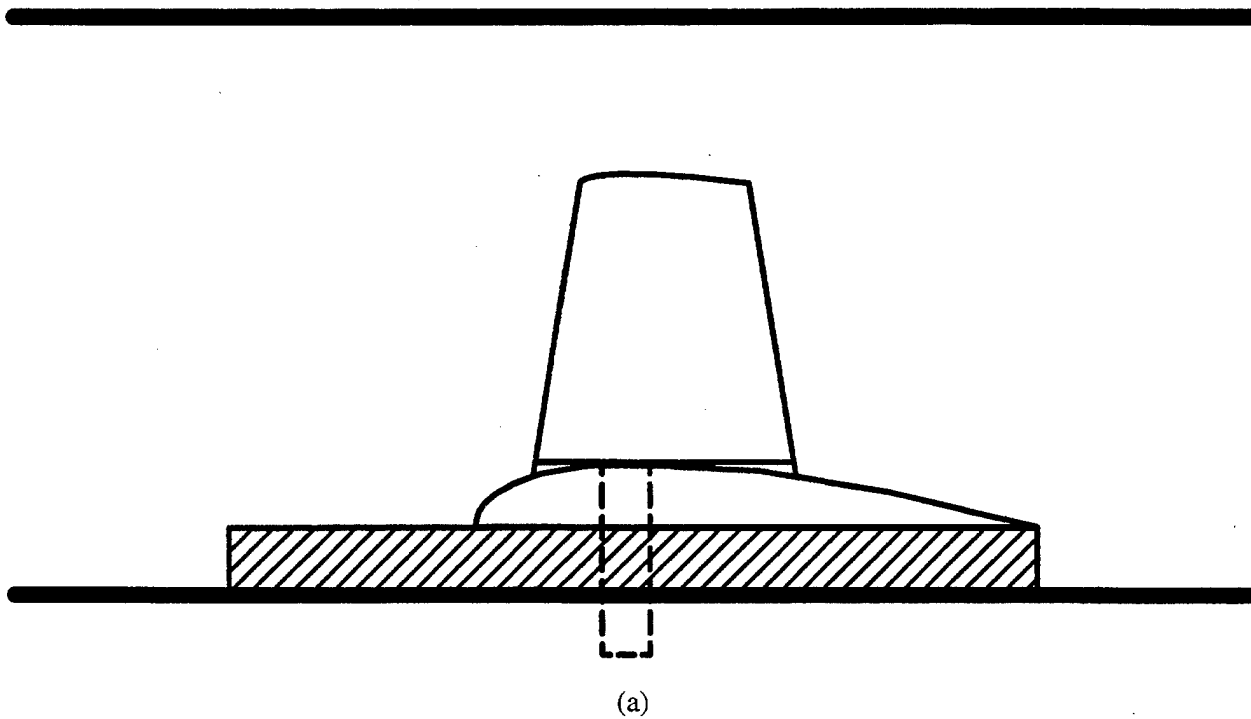
Fig. 1. Schematic of the experimental geometry (a) as seen from below and (b) as seen from upstream.
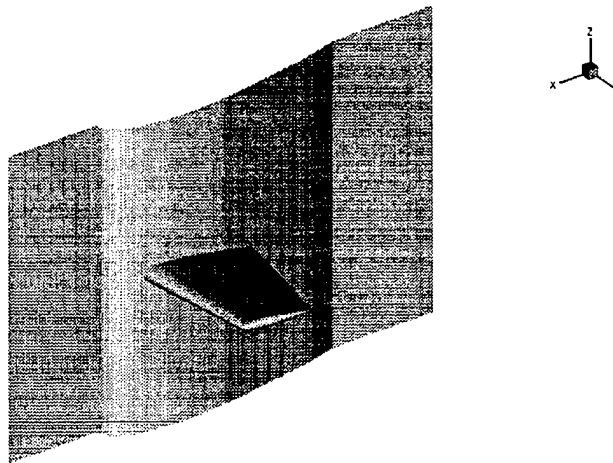
Fig. 2. Perspective view of the wing-on-wing geometric configuration used in computations.

ments taken on a coarse grid. In each plane, the experimentalists confined the grids to an area near the vortex core.

Results of the measurements are shown as contour plots in Figs. 3–6. These figures depict the nondimensional axial, spanwise, and vertical components of velocity as well as the axial component of vorticity in each of the four planes behind the wing. Results depicted for planes 1, 1A, and 2 are from measurements on the fine experimental grid. Results for plane 3, on the other hand, are from the coarse grid. The nondimensional velocity components have been scaled by the free-stream speed 26.4 ft/s. The contour plots are high-resolution views of an area near the experimentally determined position of the vortex core in each of the planes. Table 1 lists minima and maxima of items plotted in the contour plots and can be used to locate the vortex core more precisely than is possible in the contour plots.

DTNS3D

The DTNS computer codes were developed for the solution of the Navier-Stokes equations for incompressible fluid flows. These codes (DTNS2D and DTNS3D) were developed under an ONR sponsored Accelerated Research Initiative on Numerical Analysis of Naval Fluid Dynamics to meet the Navy's and NSWCCD's need for powerful general-purpose computational tools for incompressible fluid flows in a wide variety of naval geometries. The DTNS codes have proven useful in numerous applications including two-dimensional propeller and compressor blade computations, inlet computations, axisymmetric vortex breakdown, and three-dimensional ship and submarine calculations.

Only a brief description of the solution procedure is given here as details can be found elsewhere[7-11] and in Appendix A. The Navier-Stokes equations contain both first derivative convective terms and second derivative viscous terms. The viscous terms are numerically well behaved diffusion terms and are discretized using standard central differences. Third order upwind differencing is used for discretizing the convective part of the equations. Jacobian matrices associated with the convective terms are used to generate eigenvectors and eigenvalues for the system of equations. Then, based on the sign of the eigenvalues, the convective terms are differenced either forward or backward. This produces a third order accurate numerical scheme without any artificial dissipation terms being added to the equations for stability. The equations are transformed to a body-fitted coordinate system and solved using a finite volume procedure.

4

Fig. 3. Measured axial, spanwise, and vertical velocity components and axial vorticity component in plane 1.

THIS PAGE INTENTIONALLY LEFT BLANK

Fig. 4. Measured axial, spanwise, and vertical velocity components and axial vorticity component in plane 1A.

THIS PAGE INTENTIONALLY LEFT BLANK

Spanwise Velocity

0.5
0.4
0.3
0.2
0.1
0.0
-0.1
-0.2
-0.3
-0.4
-0.5

Axial Vorticity

40
0
-40
-80
-120
-160
-200
-240
-280
-320
-360

Axial Velocity

1.10
1.05
1.00
0.95
0.90
0.85
0.80
0.75
0.70
0.65
0.60
0.55

Vertical Velocity

0.5
0.4
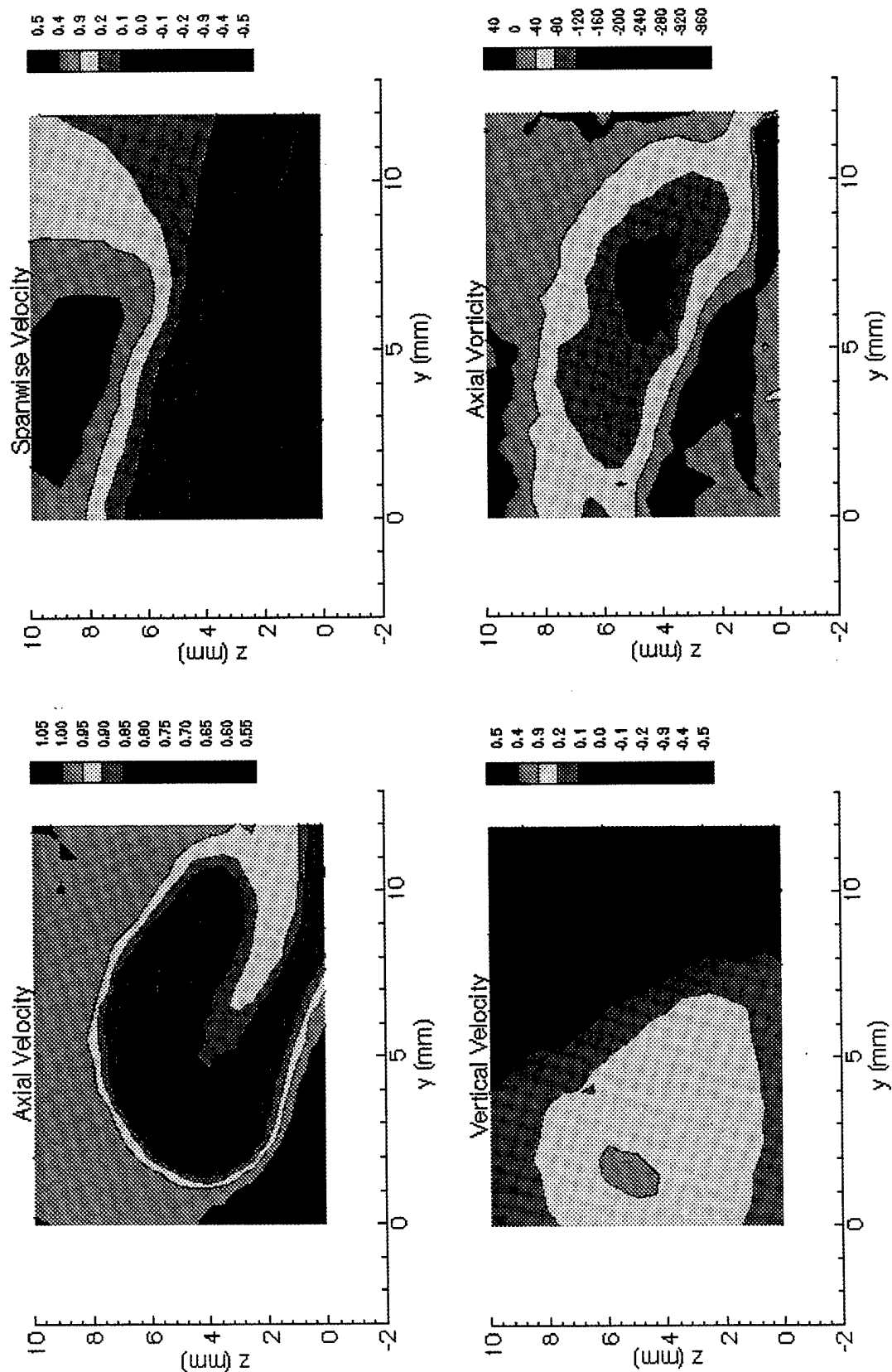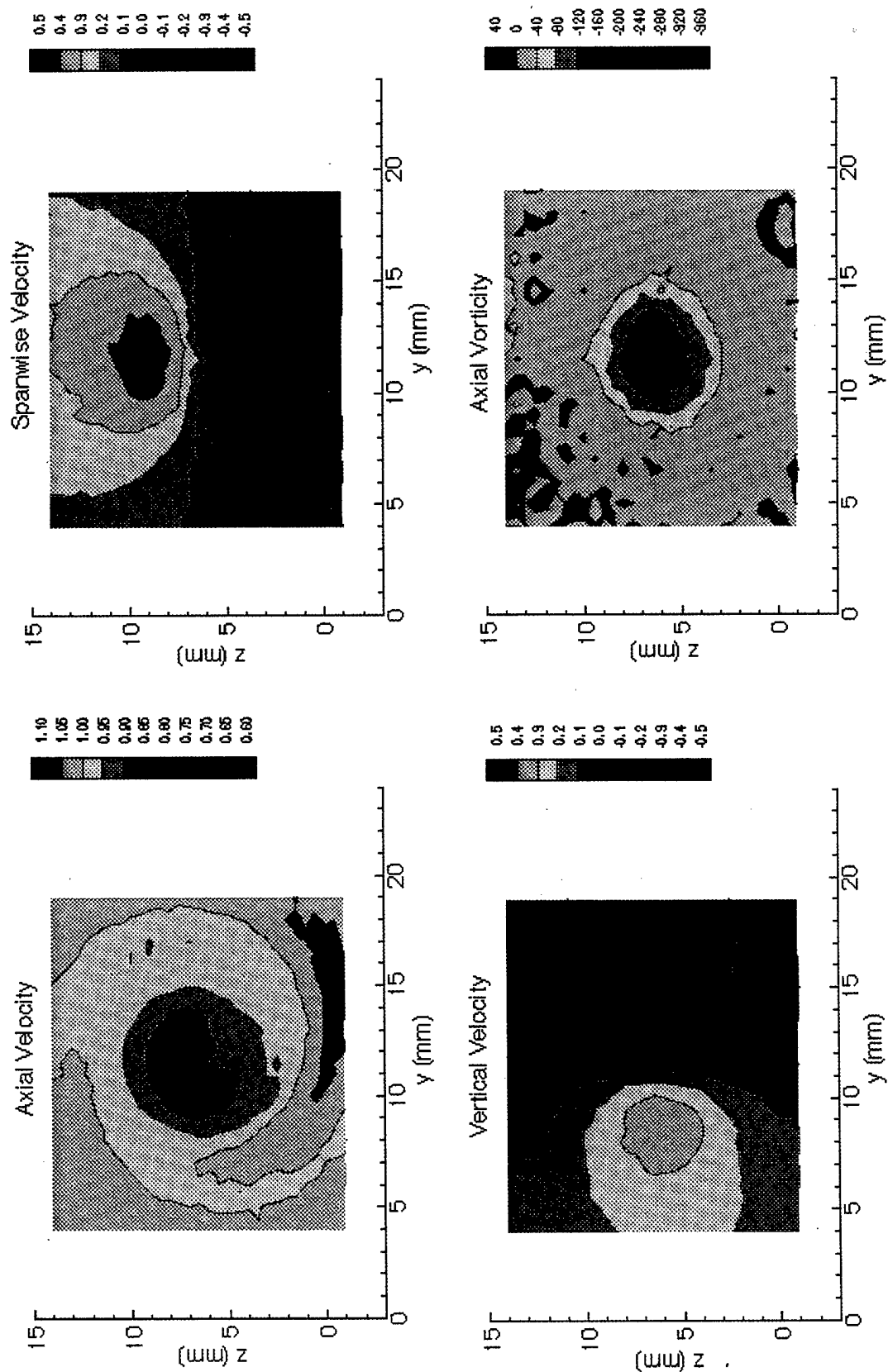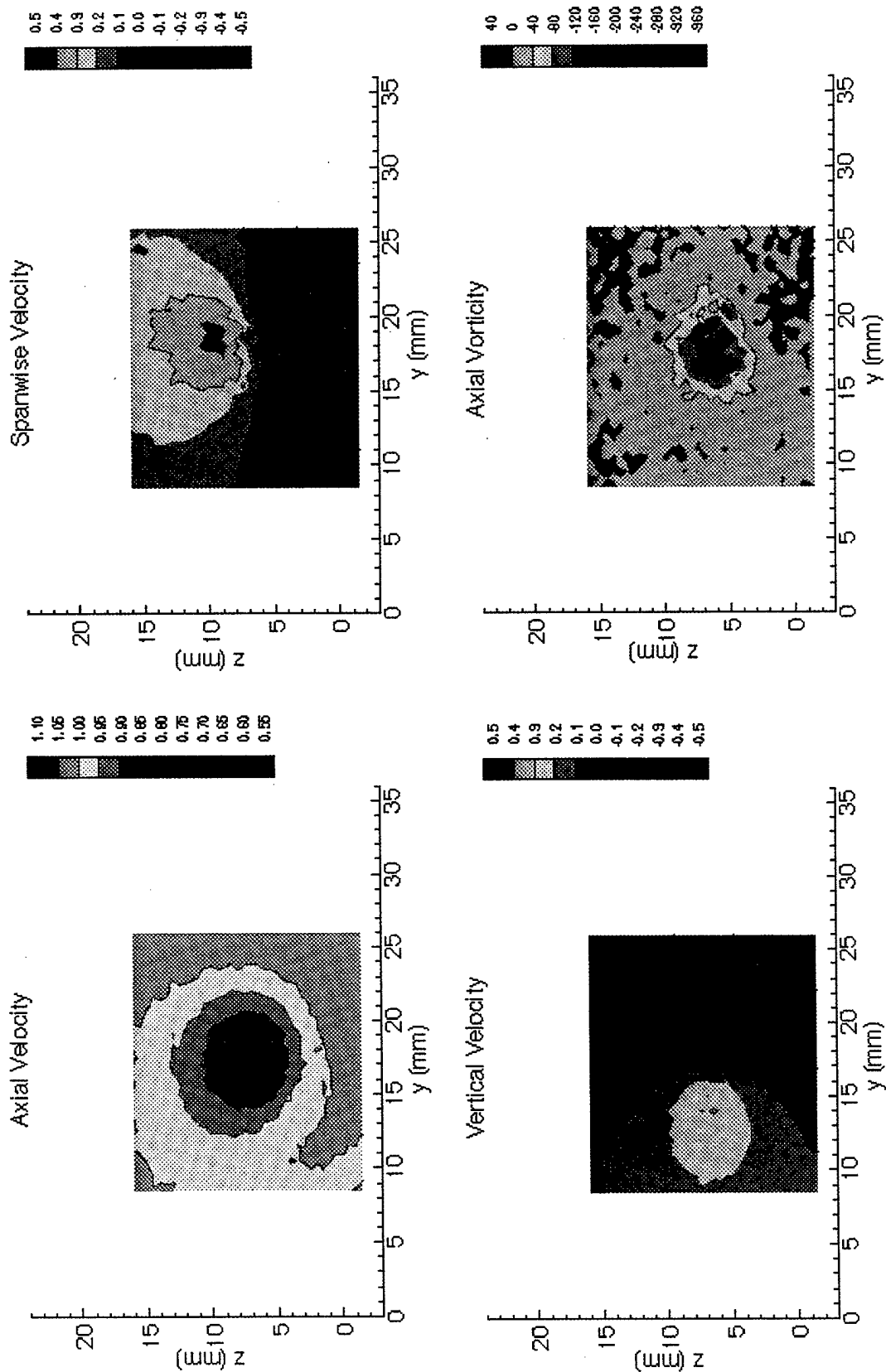0.3
0.2
0.1
0.0
-0.1
-0.2
-0.3
-0.4
-0.5

Fig. 5. Measured axial, spanwise, and vertical velocity components and axial vorticity component in plane 2.
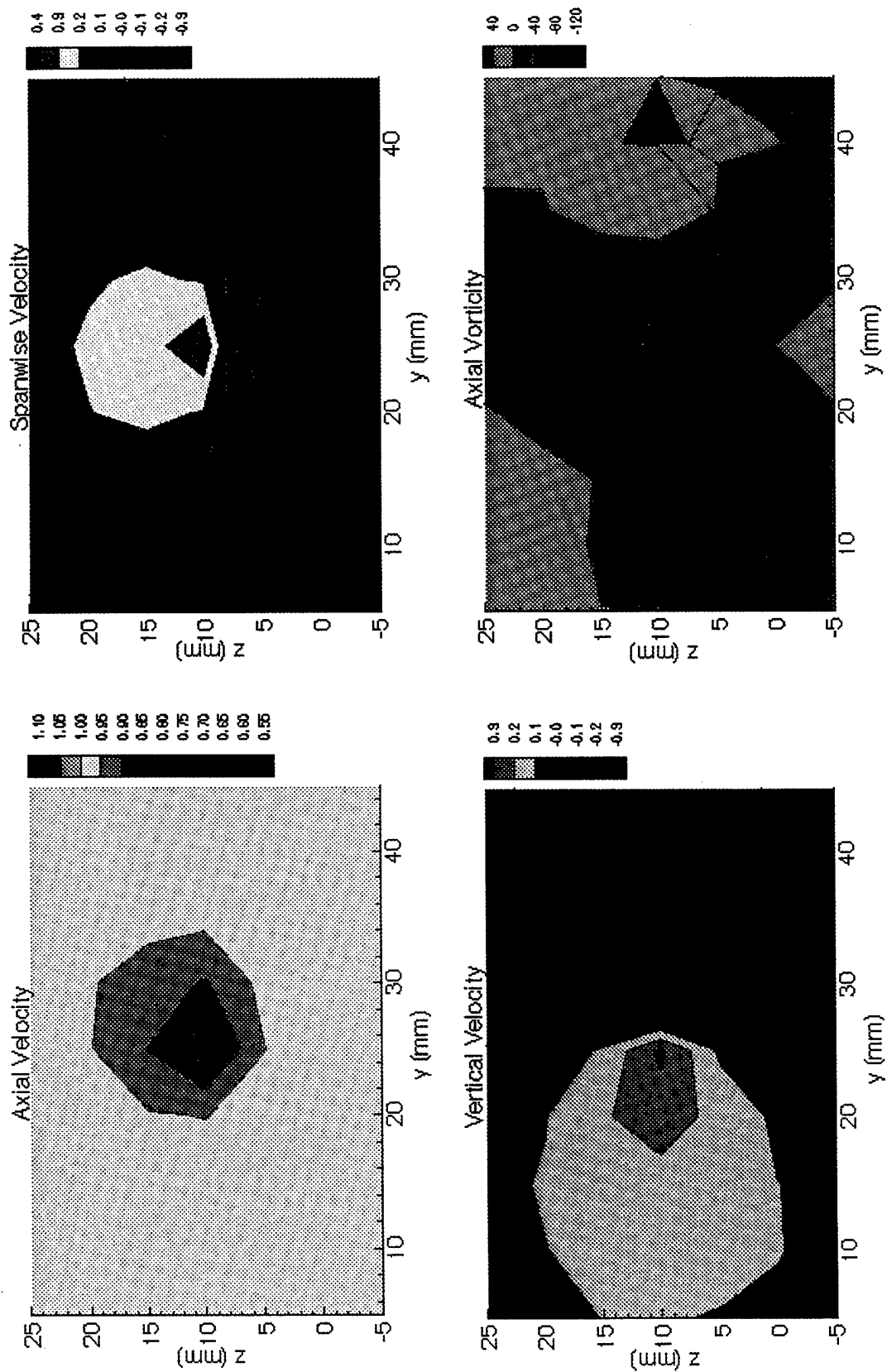
9

THIS PAGE INTENTIONALLY LEFT BLANK

Fig. 6. Measured axial, spanwise, and vertical velocity components and axial vorticity component in plane 3.

Table 1. Minima and maxima of measurements and computations.

Quantity*	Experimental Data		Computed Results			
			Baldwin-Lomax Turbulence Model Used Behind Turbulence Stimulators $U = 26.4$ ft/s (Case 1)		Baldwin-Lomax Turbulence Model Used on the Entire Wing Surface $U = 24.0$ ft/s (Case 2)	
	Location (x, y) (mm)	Value†	Location (x, y) (mm)	Value†	Location (x, y) (mm)	Value†
Plane 1						
u min	(3.5, 6.0)	0.70	(0.3, 5.2)	0.66	(−0.8, 4.0)	0.60
v min	(5.5, 2.5)	−0.41	(3.2, 1.1)	−0.46	(4.1, 0.7)	−0.45
v max	(4.0, 8.5)	0.55	(3.2, 6.1)	0.65	(3.2, 5.8)	0.63
w min	(11.5, 4.0)	−0.41	(7.0, 3.4)	−0.37	(7.0, 3.2)	−0.36
w max	(1.5, 5.0)	0.35	(1.0, 3.3)	0.60	(1.7, 2.9)	0.52
ω_x min	(6.5, 4.5)	−160	(4.1, 3.2)	−486	(4.1, 3.5)	−490
Plane 1A						
u min	(11.5, 8.0)	0.93	(9.7, 5.8)	0.66	(9.7, 4.9)	0.70
v min	(11.5, 3.0)	−0.38	(9.7, 2.2)	−0.33	(9.7, 1.5)	−0.31
v max	(11.5, 9.0)	0.51	(9.7, 9.6)	0.49	(9.7, 9.1)	0.46
w min	(14.5, 6.0)	−0.41	(13.9, 5.7)	−0.40	(13.9, 5.1)	−0.38
w max	(9.0, 6.0)	0.43	(6.2, 5.8)	0.42	(6.2, 5.3)	0.41
ω_x min	(11.5, 6.0)	−270	(9.7, 6.1)	−229	(9.7, 5.5)	−220
Plane 2						
u min	(17.0, 8.0)	0.88	(14.6, 7.3)	0.64	(14.6, 5.5)	0.63
v min	(18.0, 4.0)	−0.40	(14.6, 2.2)	−0.28	(14.6, 1.0)	−0.27
v max	(18.5, 10.0)	0.49	(14.6, 12.1)	0.42	(14.6, 10.4)	0.41
w min	(20.5, 6.5)	−0.38	(20.0, 7.2)	−0.33	(20.0, 5.9)	−0.31
w max	(14.0, 6.5)	0.34	(10.1, 6.9)	0.37	(10.1, 5.6)	0.36
ω_x min	(18.5, 5.0)	−220	(14.6, 7.3)	−149	(14.6, 6.4)	−140
Plane 3						
u min	(25.0, 10.0)	0.90	(23.5, 7.8)	0.67	(21.3, 7.1)	0.65
v min	(25.0, 5.0)	−0.32	(23.5, 1.9)	−0.24	(23.5, 0.7)	−0.23
v max	(25.0, 10.0)	0.42	(23.5, 13.6)	0.32	(21.3, 12.3)	0.31
w min	(30.0, 10.0)	−0.39	(28.3, 8.5)	−0.26	(28.3, 7.1)	−0.26
w max	(25.0, 10.0)	0.35	(21.3, 7.1)	0.12	(21.3, 7.1)	0.05
ω_x min	(25.0, 10.0)	−51	(23.5, 9.3)	−89	(21.3, 7.1)	−88

* The quantities u, v, and w, are the mean axial, spanwise, and vertical components of the velocity; ω_x is the mean axial component of vorticity.

† Values in this column are nondimensional.

The artificial compressibility technique of Chorin[12] is used to add a time derivative term for pressure to the continuity equation. This technique allows the system of equations to progress in time in an implicit coupled manner using approximate factorization. The implicit side of the equations is discretized with a first-order accurate upwind scheme for the convective terms. This scheme creates a diagonally dominant system which requires the inversion of block tridiagonal matrices. The implicit side of the equations is only first-order accurate, but the final converged solution has the high order accuracy of the explicit part of the equations.

COMPUTATIONAL GRID

A right-handed coordinate system is oriented so that the positive x–axis points upstream, the positive y–axis points away from the vertical half-thickness wing, and the positive z–axis points vertically upward. The origin is at the trailing edge of the wing tip.

The section of the tunnel for which computations are performed is restricted to $-14.7 \le x/L \le 15.2$, $-9.24 \le y/L \le 7.56$, and $-9.41 \le z/L \le 10.09$ in which L is 1 in. A computational grid was designed so that it conforms to the boundaries of the square water tunnel and the simplified horizontal wing/vertical half-thickness wing configuration attached to a tunnel wall. Figure 7 shows parts of the grid surrounding the wings in the tunnel. Here the orientation of the geometry is almost identical to that of Fig. 2.

The grid was designed so that there are approximately 30 to 40 grid points normal to the wing in the boundary layer. To obtain such a grid, the turbulent boundary-layer thickness was estimated by considering boundary-layer thickness on a flat plate aligned with the flow. An estimated turbulent boundary-layer thickness of 1.1×10^{-4} in. was obtained. To keep the number of grid points manageable, the grid spacing near the half-body and the tunnel walls was relatively coarse compared to the grid spacing used on the wing. In particular, boundary layers on these boundaries cannot be resolved using this grid. A slip boundary condition was specified for the flow calculations here. Use of the slip boundary condition permitted modeling the correct mass flow blockage with a reduced number of grid points. These boundaries are relatively far from the tip vortex, the feature of interest in the flow calculations.

The grid consists of nine blocks depicted in the expanded view of the mesh in Fig. 8. In this figure the blocks have been separated from one another. Three blocks of the computational grid are in direct contact with the wing. Block 2 lies directly above the wing, block 5 lies directly below the wing, and block 8 connects these blocks. Block 8 is in contact with the wing only near the tip. These three blocks extend out to the tunnel walls. The grid spacing within these blocks expands from fine in the boundary layer on the wing to coarse at the tunnel walls. The grid spacing near the half-body is coarser than it is at the wing tip. The central transverse section in Fig. 7a shows a section of these three blocks. Three blocks lie at the upstream end of the computational region ahead of the wing. Block 1 lies forward of block 2, block 4 is forward of block 5, and block 7 lies ahead of block 8. Blocks 1 and 4 have a common, nearly horizontal computational surface grid. One of the computational faces of block 7 collapses onto a line segment upstream of the wing tip. The remaining three blocks lie downstream of the wing. Block 3 is downstream from block 2, block 6 is downstream of block 5, and block 9 lies downstream of block 8. Blocks 3 and 6 share a common computational surface grid. One face of block 9 collapses onto a line segment downstream of the wing tip. A transverse section of the downstream blocks is depicted in Fig. 7a. Table 2 lists the size of each of the nine blocks forming the computational grid. There are almost 1.7 million grid points.

Table 2. Computational blocks.

Block No.	Grid Size $(l_{dim} \times k_{dim} \times j_{dim})$
1	$49 \times 81 \times 25$
2	$49 \times 81 \times 61$
3	$49 \times 81 \times 81$
4	$49 \times 81 \times 25$
5	$49 \times 81 \times 61$
6	$49 \times 81 \times 81$
7	$27 \times 81 \times 25$
8	$27 \times 81 \times 61$
9	$27 \times 81 \times 81$
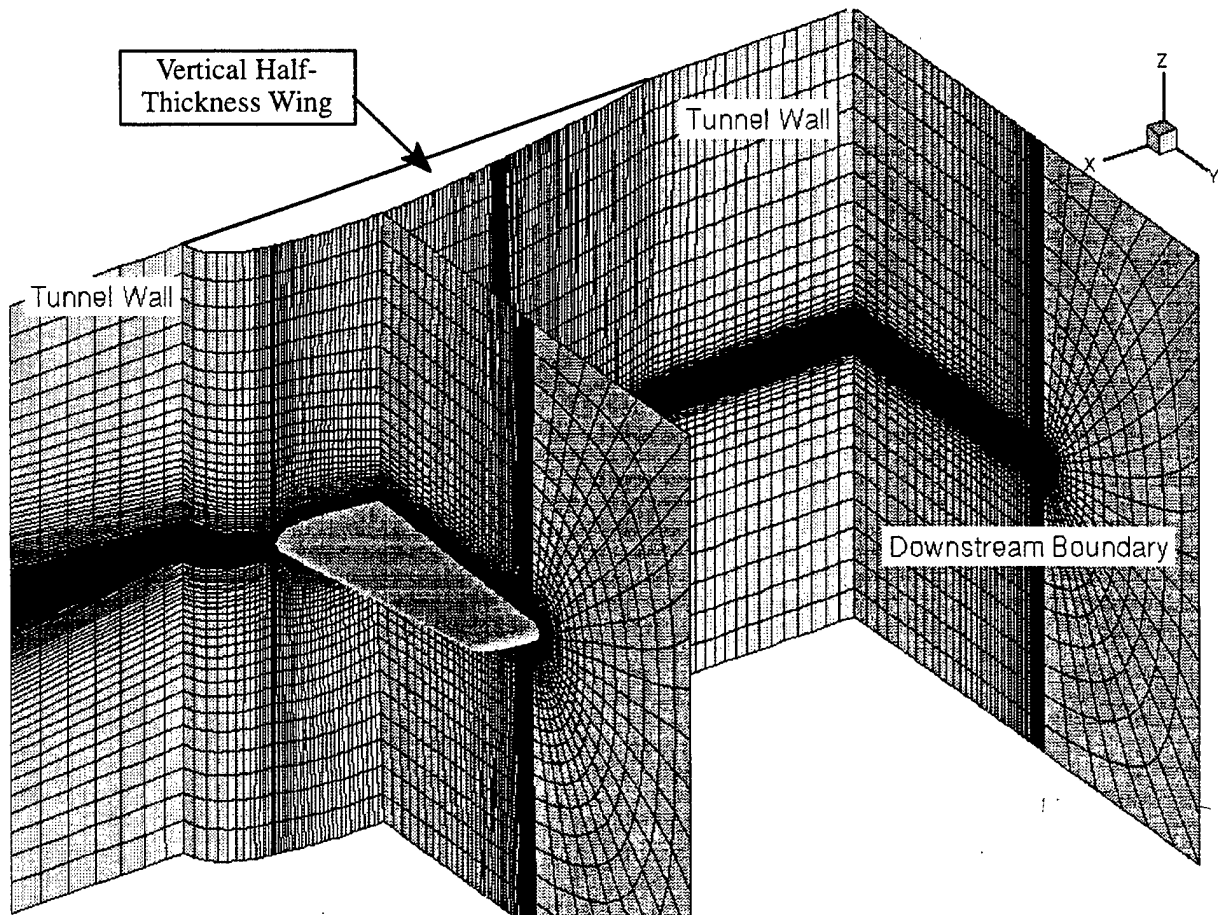
Fig. 7a. The computational grid along the tunnel wall, the vertical half–thickness wing, the downstream boundary, and a section intersecting the horizontal wing.

Fig. 7. Perspective view of parts of the computational grid.

14
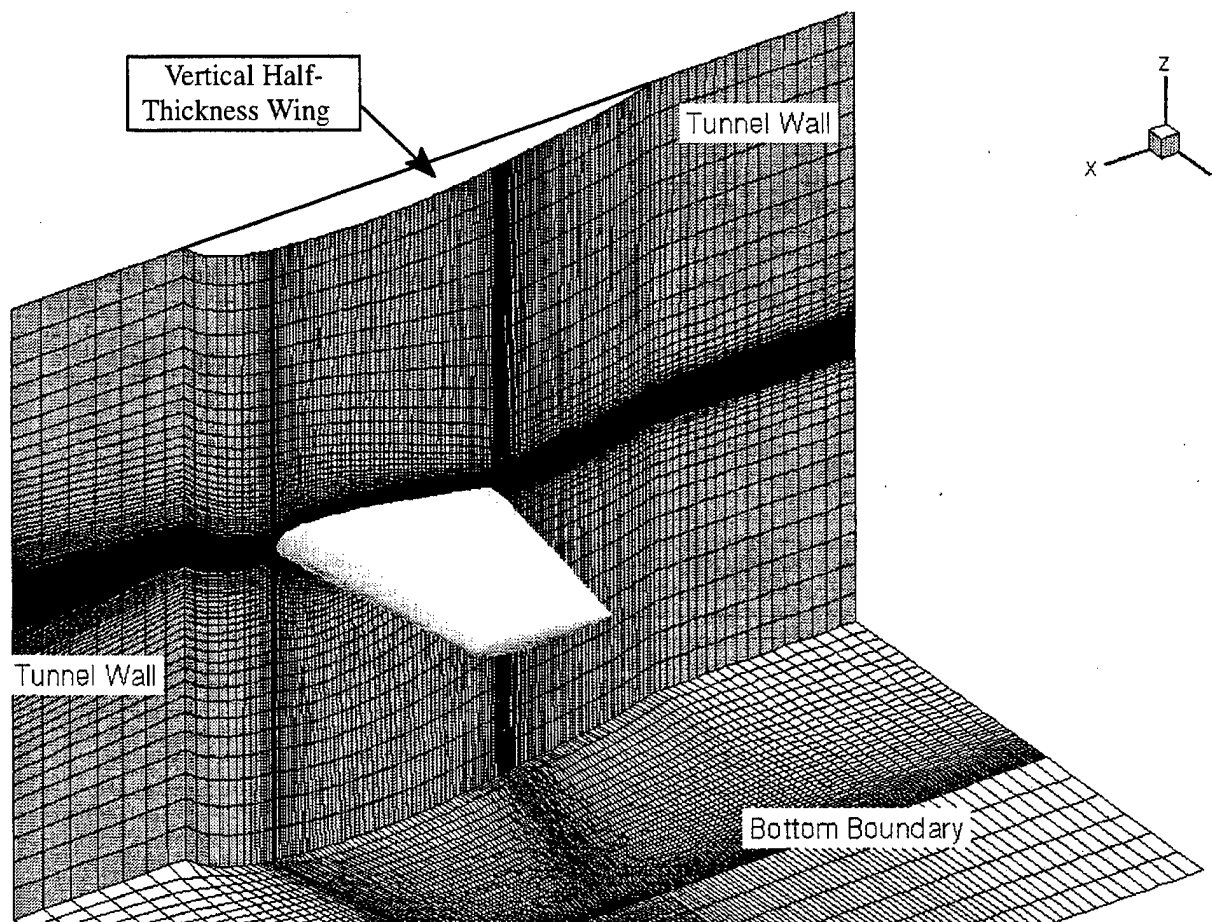
Fig. 7b. The computational grid along the tunnel wall
and the bottom of the computational region.

Fig. 7. (Continued)

Figure 9 shows where measurements were taken in each of the planes 1, 1A, 2, and 3. The locations of the measurement grids are plotted alongside the wing-on-wing configuration. This figure also shows the computational grid on the horizontal wing.

The DTNS3D computer program requires the specification of a boundary condition on each of the six faces of a computational block. Where blocks meet inside the computational region, a high-accuracy matching boundary condition was specified. A slip boundary condition was specified on tunnel walls and on the vertical half-body. Upstream and downstream boundary conditions were specified on computational faces at the upstream and downstream ends of the computational region. Only on the wing was a no-slip boundary condition specified.

COMPUTATIONAL RESULTS

Computational results are presented for the Baldwin-Lomax turbulence model. The speed of the uniform flow was set to 26.4 ft/s. Transition from a laminar to a turbulent boundary layer was enforced at a distance of approximately 20 percent of the local chord behind the leading edge of the horizontal wing, the position at which turbulence stimulators were placed in the experiment. To simplify the coding, the transition to turbulence was enforced by setting all turbulence quantities to zero ahead of the $j = 17$ com-

15
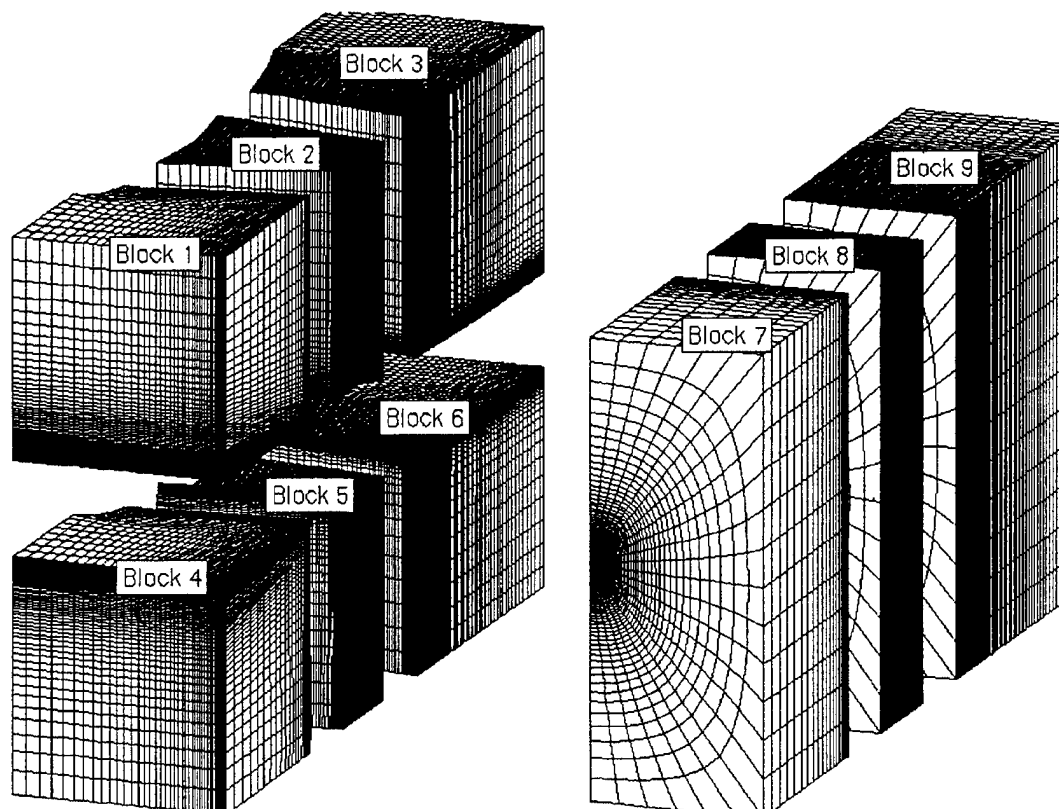
Fig. 8. Expanded view of the computational grid.

putational plane. Figure 10 shows the line along which transition to turbulence was enforced on the upper surface of the wing. A similarly placed line on the lower surface of the wing would indicate where transition to turbulence was enforced on that surface.

A second set of results is presented in Appendix B for the case in which the boundary layer is assumed to be turbulent over the entire wing surface and the speed of the uniform stream is 24.0 ft/s instead of 26.4 ft/s. In Appendix B, boundary layer profiles at points shown in Fig. 10 are plotted to demonstrate convergence of the computed solution of Appendix B.

In both cases, the initial flow was set to uniform stream flow. The computer program then progressed through a sequence of pseudotime steps. The CFL (Courant–Friedrichs–Lewy) number, which relates the flow speed, the grid spacing, and the time step and which is used to determine the local time step, was set to 2.0.

For the most part, computations were performed on a CONVEX C220 and a CONVEX C3840 at NSWCCD. The amount of time required to produce these results is on the order of months. Computations were carried out continually during this period. Some results were obtained by continuing computations on a CRAY C90 from a nearly converged solution obtained on the CONVEX C3840.

Computational results are depicted in the form of contour plots in each of the four measurement planes downstream of the trailing edge of the horizontal wing. Figure 9 shows a perspective view of where the measurement planes are with respect to the wing-on-wing geometry.

Figures 11 through 14 show contour plots of three components of velocity and the axial component of vorticity. These are plots of computed data in the four measurement planes. The middle columns of Table 1 labeled Case 1 list the corresponding maxima and minima of various quantities related to the
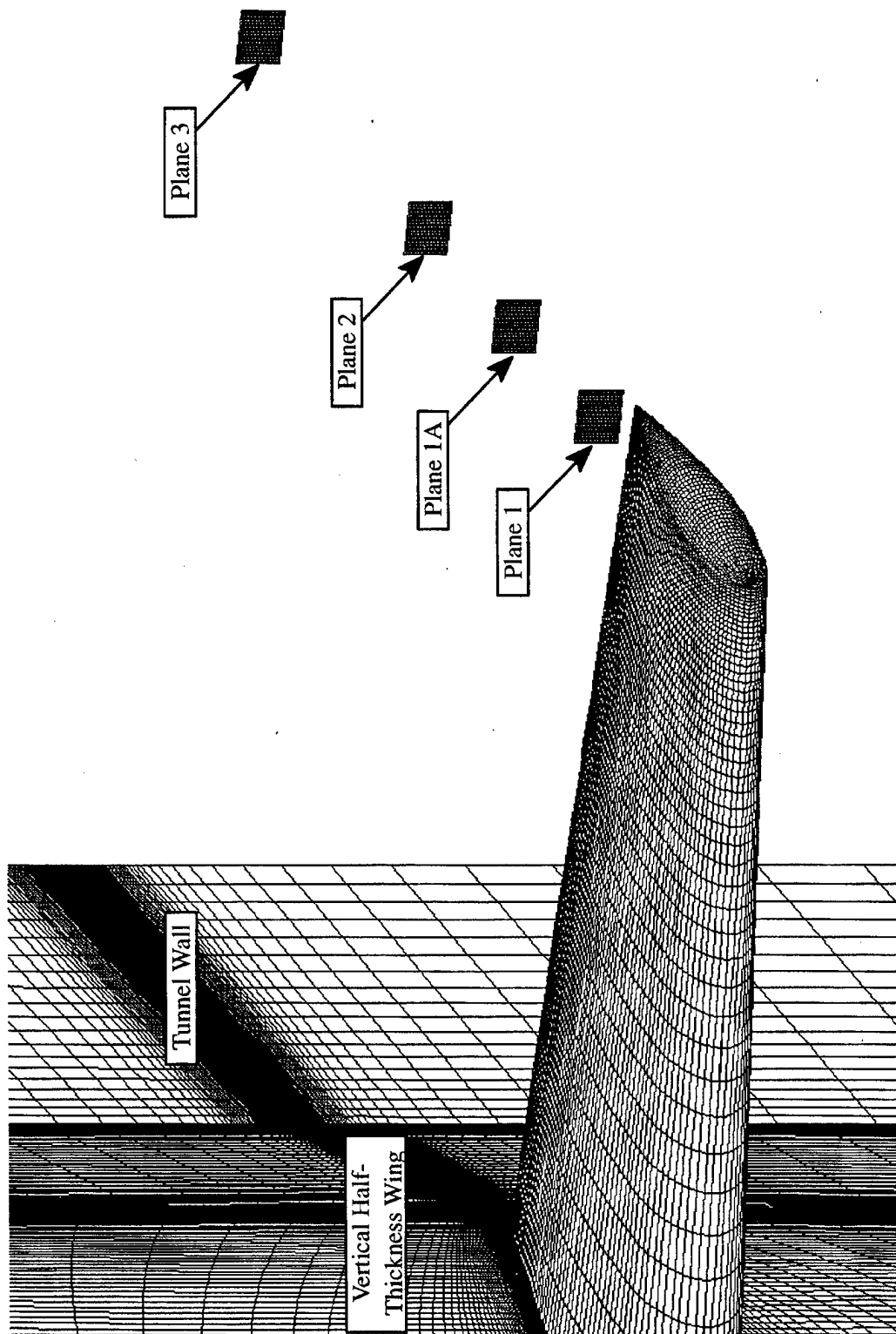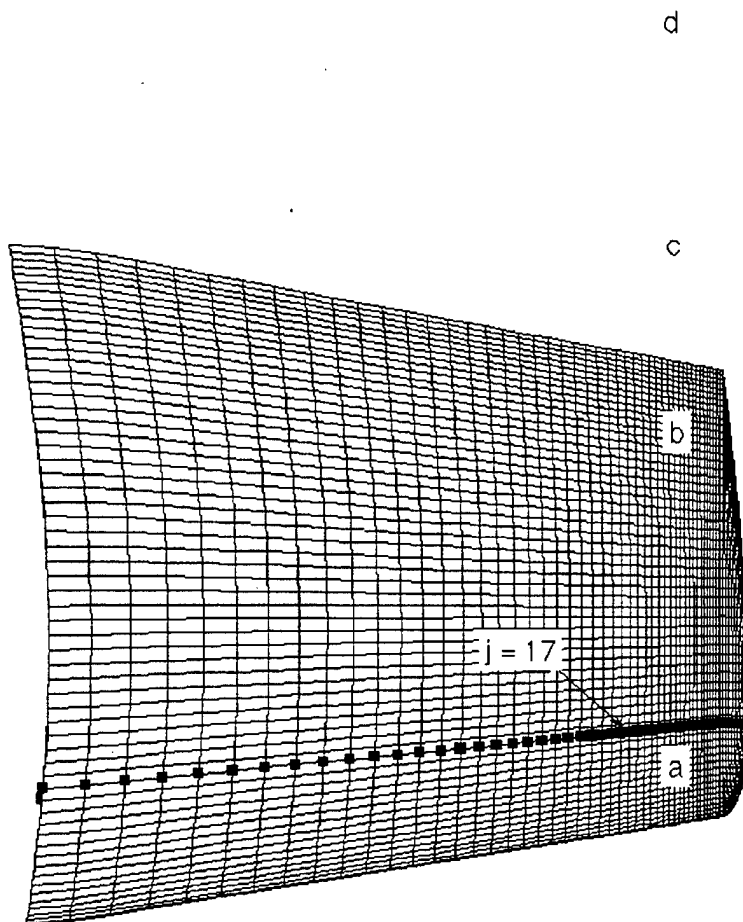
16

Fig. 9. Locations of the four measurement planes plotted alongside the geometry of the wing-on-wing configuration.

Fig. 10. Locations (a)-(d) at which boundary-layer profiles of the mean stream-
wise velocity were monitored and the approximate location of transition
to turbulence in experiments.

position of the core of the tip vortex in each of the four planes. A postprocessing computer program was used to search for the numbers listed in the table.

By comparing the contour plots of the computed and measured streamwise component of the mean velocity for plane 1 (9 mm behind the trailing edge) shown in Figs. 3 and 11, it is apparent that the computed position of the core is shifted outward from the experimentally determined position. More precise information listed in Table 1 shows that the horizontal shift is about 3 mm. The data for the stream-wise component of the mean velocity listed in the table also show that there is a downward shift in the computed position of the core from the experimentally determined position. The downward shift is slightly less than 1 mm. Because the average chord is about 150 mm, the shift in core position is about 2 percent of the chord of the wing. The shapes of the measured and numerically obtained streamwise velocity contours are similar. The computed size of the core region compares well with the experimentally determined core size. The nondimensional streamwise velocity assumes a nondimensional minimum value of 0.66 while measurements indicate that the minimum should be 0.70. Computed and measured values of spanwise and vertical velocities in plane 1 are compared in the same figures. The minima of these nondimensional velocity components, listed in Table 1, differ by at most 0.05, which is approximately 12
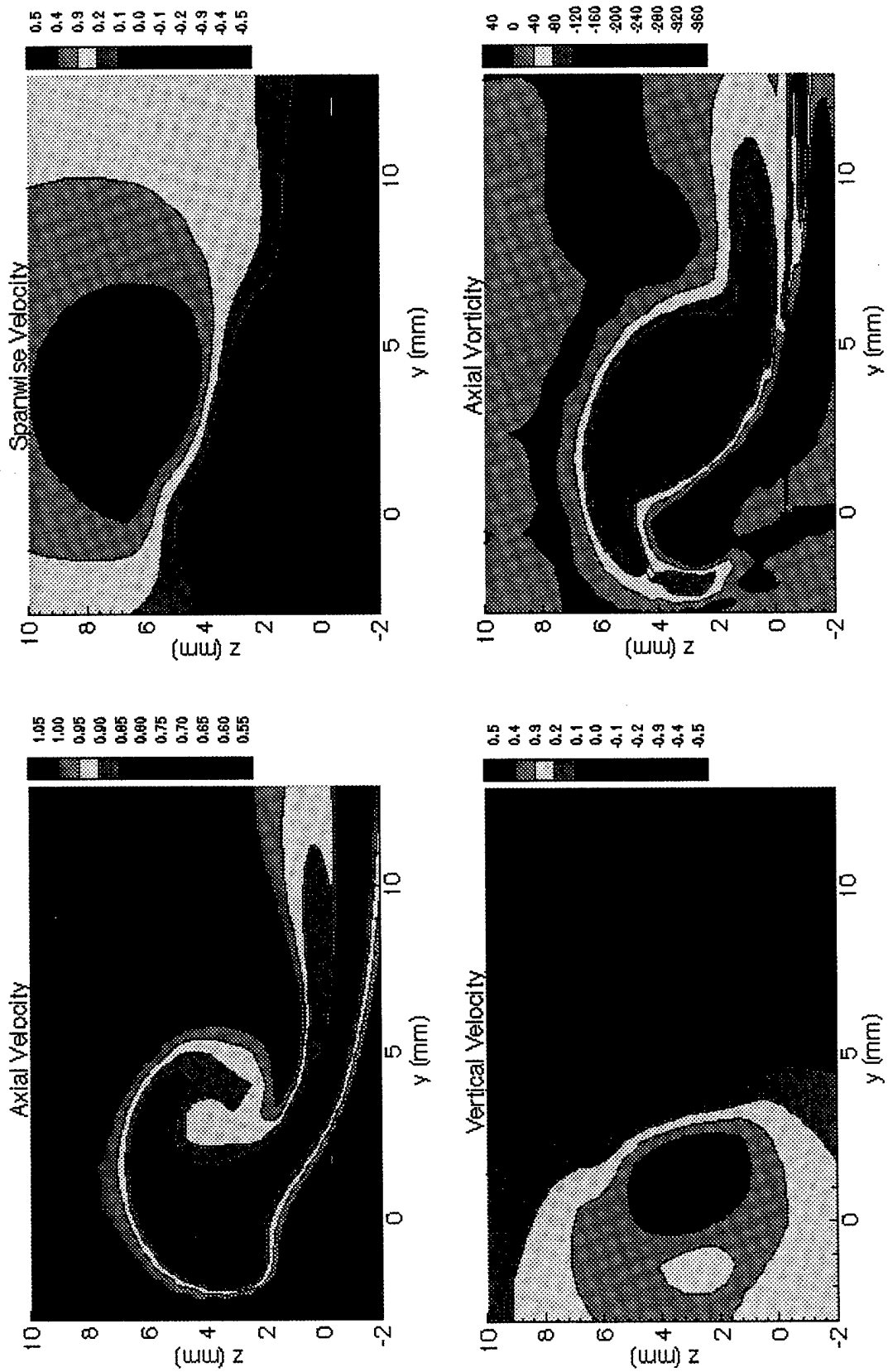
Fig. 11. Computed axial, spanwise, and vertical velocity components and axial vorticity component in plane 1 for $U = 26.4$ ft/s.

19

THIS PAGE INTENTIONALLY LEFT BLANK
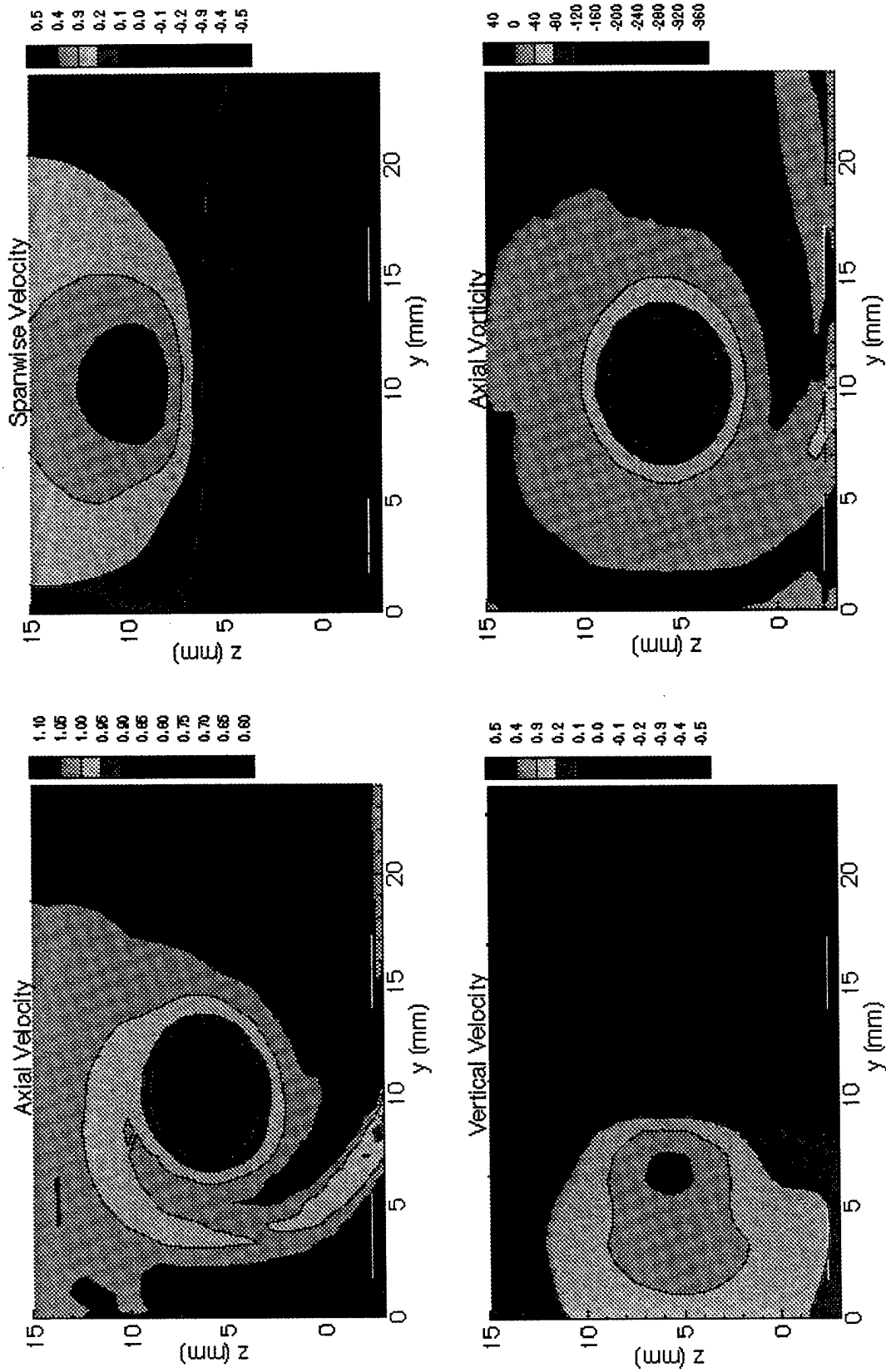
Fig. 12. Computed axial, spanwise, and vertical velocity components and axial vorticity component in plane 1A for $U = 26.4$ ft/s.
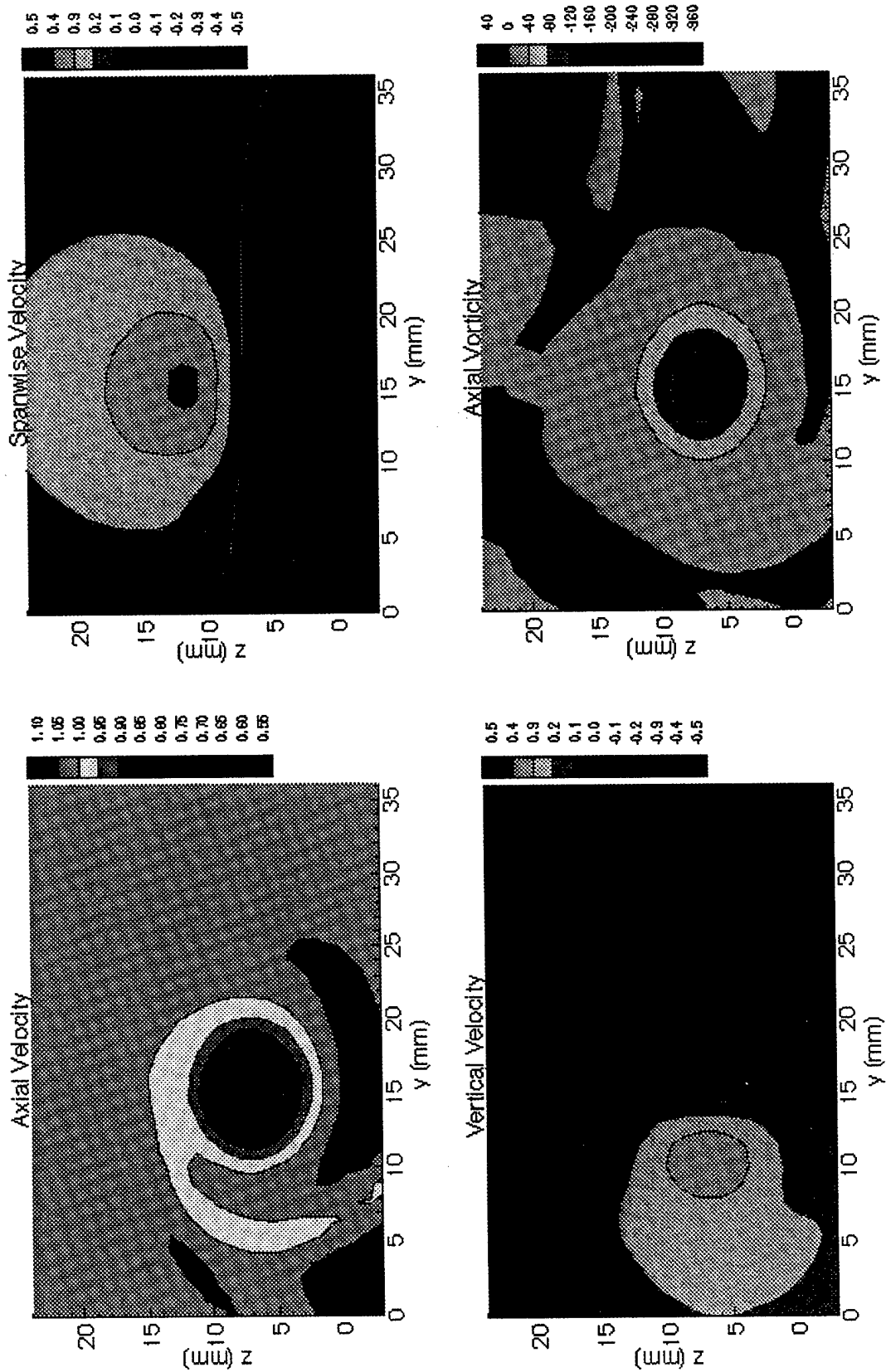
THIS PAGE INTENTIONALLY LEFT BLANK

Fig. 13. Computed axial, spanwise, and vertical velocity components and axial vorticity component in plane 2 for $U = 26.4$ ft/s.
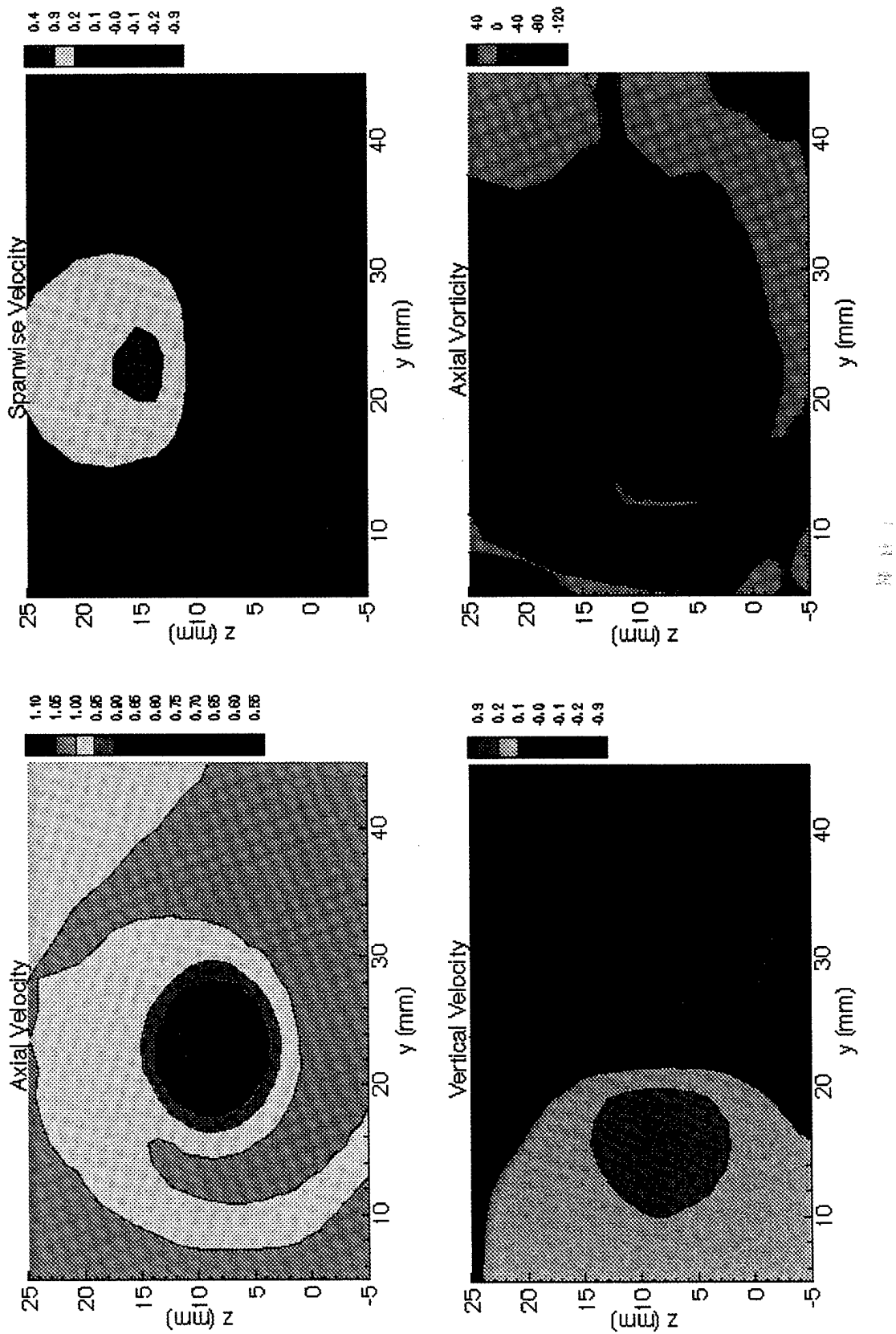
THIS PAGE INTENTIONALLY LEFT BLANK

Fig. 14. Computed axial, spanwise, and vertical velocity components and axial vorticity component in plane 3 for $U = 26.4$ ft/s.

percent. The maxima differ to a greater extent. Specifically, the difference for the spanwise component is 18 percent, and the difference for the vertical component is 71 percent.

The remaining set of results plotted in Figs. 3 and 11 is the axial component of vorticity in plane 1. The axial component of vorticity was not computed directly by DTNS3D. Instead, computed values of the axial, spanwise, and vertical components of velocity at discrete points related to the computational grid were differenced in a postprocessing computer program to obtain the vorticity. Similarly, for the experimental measurements, the vorticity was obtained by differencing components of velocity on the grid of points at which measurements were made. Hence, both the measured and computed values of vorticity are less accurate than the values of components of velocity.

The computed and measured axial velocity components for plane 1A (70 mm behind the trailing edge) are shown in Figs. 4 and 12. As was the case for plane 1, there is an outward and downward shift in the computed position of the vortex core from the measured position of the core. If the minimum of the axial component of velocity indicates the position of the vortex core, then the data of Table 1 imply that the shift in vortex core position both horizontally and vertically is about 2 mm. The minimum of the nondimensional mean streamwise velocity in the core is underpredicted by 29 percent. The computed minimum is 0.66 while the measured minimum is 0.93. Nondimensional measured and computed spanwise and vertical velocity components can also be compared. For these velocity components, the calculated minimum is within 0.05 (at most 13 percent) of the measured minimum, and the calculated maximum is within 0.02 (about 4 percent) of the measured maximum.

Figures 5 and 13 compare measurements and computations in plane 2 (136 mm behind the trailing edge). Table 1 lists the maxima and minima of the flow variables plotted in these figures. Based on the minimum of the nondimensional axial velocity, the computed position of the vortex core is 2.4 mm further out and 0.7 mm lower than the measured position. The computed minimum in the nondimensional mean streamwise velocity component is 0.64, which is 27 percent lower than the experimentally determined value of 0.88. Agreement between the measured and computed minimum of the mean spanwise velocity component is somewhat worse than it is for plane 1A; they differ by 0.12 (roughly 30 percent). The measured and computed maximum of the mean spanwise velocity differ by 0.07 (14 percent). For the minimum and maximum of the vertical velocity the agreement is slightly worse than it is for plane 1A. These quantities differ by at most 0.05 (13 percent).

Details of measurements and computations for plane 3 (263 mm downstream from the trailing edge of the wing) are depicted in Figs. 6 and 14. Table 1 gives maxima and minima of computed mean flow variables in this plane. Here, unlike the case for the other three planes, experimental data are available only on the coarse grid. Minima and maxima of experimental data on the coarse grid are listed in the first columns of the table. The shift in the position of the vortex core that was noted in the three planes closer to the wing persists. Based on the data for the mean axial velocity, the outward and downward shifts in the computed position of the core are about 1.5 and 2.2 mm, respectively. As is the case for planes 1A and 2, the computed minimum of the mean streamwise velocity is low; in this plane, by about 26 percent.

CONCLUSIONS

For the numerical calculations presented in this report, the position of the tip-vortex core is computed fairly well. The calculated position is somewhat low and further out from the vertical wing attached to the tunnel wall than the measurements indicate. The discrepancy between the measured and computed position of the core in each of the four planes in which measurements were made in the MIT experiment is less than 2 percent of the mean chord of the horizontal wing.

In general, there is insufficient information available about the use of turbulence models near the tip of a wing. A number of turbulence models have been developed through the years. However, it is not clear which turbulence model is appropriate for the generation and propagation of the tip vortex downstream of the wing in the wake. Furthermore, three-dimensional turbulence models are usually developed in the absence of walls. As a result, it may be difficult to apply the latest models to the problem of tip-vortex generation and propagation. If such models show little sensitivity to flow boundaries, the newer models may not be adequate when the fluid interacts with these boundaries to produce phenomena such as tip vortices.

The eddy viscosity for the Baldwin-Lomax turbulence model, as can be seen from the contour plot of it in Appendix B, does not seem reasonable. The contour plot in Appendix B corresponding to the use of the k-ϵ turbulence model instead of the Baldwin-Lomax turbulence model is reasonable. Any conclusion based on these figures must be tentative since the computations for the k-ϵ turbulence model were terminated before convergence was attained.

Part of the difference between the computed and measured position of the vortex core may arise from not knowing precisely where the transition from a laminar to a turbulent boundary layer occurs. In experiments, the position of the turbulence stimulators is known, but it is not unheard of for transition to occur upstream of turbulence stimulators.

The discrepancy in the measured and computed positions of the vortex core may also demonstrate the effect of reducing the number of grid points in the computational grid so that a numerical solution on the grid could be generated in a reasonable time. First, the pedestal was not modeled. If the pedestal was modeled, then some vortex rollup would have occurred at the junction of the wing and pedestal. Lack of a modeled pedestal may, in turn, affect the amount of vorticity in the rollup at the tip and the position of the core of the tip vortex. The effect of the absence of the pedestal should be greater downstream than near the tip of the wing. Second, large grid spacing was used near the vertical half-wing to limit the number of grid points. Because of the large grid spacing, a potential flow boundary condition was imposed on this boundary. The horseshoe vortex cannot, therefore, be modeled well. The effect should be as significant as the absence of the pedestal in the numerical model.

In the interest of further validating DTNS3D, additional measurements might be made. Measurements could be taken in regions outside the core of the tip vortex. A comparison of computed and measured results would ensure that DTNS3D is computing correctly in regions where the flow is less active than it is in the core region. Measurements might be taken for the case of completely laminar flow, and the corresponding computations made. A comparison would be useful in further verification of the use of RANS codes for this flow problem. If laminar flow cannot be computed correctly, there is little assurance that results obtained from using turbulent flow models are reasonable.

ACKNOWLEDGMENTS

THIS PAGE INTENTIONALLY LEFT BLANK

APPENDIX A
REYNOLDS AVERAGED NAVIER-STOKES EQUATIONS

DTNS3D solves the full Reynolds Averaged Navier-Stokes (RANS) equations with a turbulence model. Only incompressible flow with no temperature variation is considered. For turbulent flow the pressure and the three velocity components for the Cartesian coordinate system (x, y, z) are decomposed into the sum of a mean quantity and a fluctuating quantity: $P + p$, $U + u$, $V + v$, and $W + w$. Here, an upper case letter designates a mean flow quantity, and a lower case letter designates a fluctuating quantity. Further, all quantities are nondimensionalized. Velocities are nondimensionalized with respect to the free-stream speed U_∞ and lengths by a characteristic length L. The characteristic length and speed define a Reynolds number $R_e = U_\infty L / \nu$ in which ν is the kinematic viscosity of the fluid.

For incompressible flow, the RANS equations can be written in the conservative form

$$\frac{\partial \vec{q}}{\partial t} + \frac{\partial (\vec{f}_1 - \vec{g}_1 + \vec{h}_1)}{\partial x} + \frac{\partial (\vec{f}_2 - \vec{g}_2 + \vec{h}_2)}{\partial y} + \frac{\partial (\vec{f}_3 - \vec{g}_3 + \vec{h}_3)}{\partial z} = 0 .$$

This equation includes the dependent variable $\vec{q}$, inviscid fluxes, viscous fluxes, and Reynolds stresses. The dependent variable $\vec{q}$ is given by

$$\vec{q} = \begin{bmatrix} P \\ U \\ V \\ W \end{bmatrix} .$$

The inviscid fluxes are given by

$$\vec{f}_1 = \begin{bmatrix} U \\ U^2 + P \\ UV \\ UW \end{bmatrix}, \quad \vec{f}_2 = \begin{bmatrix} V \\ UV \\ V^2 + P \\ VW \end{bmatrix}, \quad \text{and} \quad \vec{f}_3 = \begin{bmatrix} W \\ UW \\ VW \\ W^2 + P \end{bmatrix} .$$

The viscous fluxes are given by

$$\vec{g}_1 = \frac{1}{R_e} \begin{bmatrix} 0 \\ \partial U/\partial x \\ \partial V/\partial x \\ \partial W/\partial x \end{bmatrix}, \quad \vec{g}_2 = \frac{1}{R_e} \begin{bmatrix} 0 \\ \partial U/\partial y \\ \partial V/\partial y \\ \partial W/\partial y \end{bmatrix}, \quad \text{and} \quad \vec{g}_3 = \frac{1}{R_e} \begin{bmatrix} 0 \\ \partial U/\partial z \\ \partial V/\partial z \\ \partial W/\partial z \end{bmatrix} .$$

The Reynolds stresses are given by

$$\vec{h}_1 = \begin{bmatrix} 0 \\ \overline{uu} \\ \overline{uv} \\ \overline{uw} \end{bmatrix}, \quad \vec{h}_2 = \begin{bmatrix} 0 \\ \overline{vu} \\ \overline{vv} \\ \overline{vw} \end{bmatrix}, \quad \text{and} \quad \vec{h}_3 = \begin{bmatrix} 0 \\ \overline{wu} \\ \overline{wv} \\ \overline{ww} \end{bmatrix} ,$$

in which the overbars signify mean values of fluctuating quantities.

The RANS equations are transformed to a boundary-fitted coordinate system using generalized curvilinear coordinates $\xi = \xi(x,y,z)$, $\eta = \eta(x,y,z)$, and $\zeta = \zeta(x,y,z)$ where time is not among the dependent variables because the grid is fixed. After transformation, the equations can be reduced to equations of the same form as before transformation.

The convective terms $\vec{f}_1$, $\vec{f}_2$, and $\vec{f}_3$ are modeled numerically using third order upwind differencing. The terms $\vec{g}_1$, $\vec{g}_2$, and $\vec{g}_3$ are viscous diffusion terms modeled numerically using central differences.

The Reynolds stresses are modeled by replacing the molecular viscosity ν with the sum of the eddy viscosity ν_t' and the molecular viscosity. In the nondimensional equations, this is equivalent to replacing $1/R_e$ with $(1 + \nu_t)/R_e$ where $\nu_t = \nu_t'/\nu$ is the nondimensional eddy viscosity. This is basically an approximation to the Boussinesq eddy viscosity assumption

$$\overline{u_i u_j} = \frac{2}{3} k \delta_{ij} - 2\nu_t \left(\frac{\partial U_i}{\partial x_j} + \frac{\partial U_j}{\partial x_i} \right) .$$

In this equation, k is the turbulent kinetic energy, δ_{ij} is the Kronecker symbol, and indicial notation has been used for the mean velocities, the fluctuating velocities, and the coordinates. In DTNS3D, eddy viscosity can be computed using either the Baldwin-Lomax or the k-ϵ turbulence model. What is referred to as the Baldwin-Lomax turbulence model is originally due to Cebici et al.[13] It was later modified by Baldwin and Lomax[11] to avoid having to find the edge of the boundary layer.

APPENDIX B
## COMPUTATIONAL RESULTS FOR DIFFERENT FLOW CONDITIONS

Computations were also made for a set of flow conditions different from those corresponding to the main results of this report. For convenience Case 1 will refer to the main results of this report. Those results are for a uniform flow whose speed was 26.4 ft/s. Transition to turbulence was enforced at the 20 percent local chord position. Case 2 will refer to the results presented in this appendix. For Case 2 the speed of the uniform flow was 24.0 ft/s and the boundary layer was turbulent on the entire surface of the wing.

Figures 15 through 18 can be compared with Figs. 11 through 14 to see how the different speeds of uniform flow and the different positions of transition to turbulence in the boundary layer affect the computed solution. Figures 15 through 18 contain contour plots of mean velocity components and the axial component of vorticity in the four measurement planes for Case 2. The last three columns of Table 1 list maxima and minima of flow quantities obtained from these calculations. The data in the middle three columns (Case 1) and the last three columns (Case 2) for the axial component of mean streamwise velocity indicate that the computed position of the vortex core is indeed changed by the change in flow parameters. Case 2 shows a downward and outward shift of the vortex core from the position computed for Case 1. In addition, the minimum value of the mean axial velocity in the core was more underpredicted in Case 2 than it is in Case 1.

Profiles of the mean streamwise velocity component at several points on the wing and in the wake were monitored to determine how well computed results were progressing toward convergence in various regions of the flow domain. The relative positions of these points on and behind the wing are depicted in Fig. 10. Such profiles are shown in Figs. 19 through 22 for five times near the end of the computation. These times are separated by approximately 500 time steps. Because there is little change in the profiles, convergence is indicated.

Contour plots of the eddy viscosity in the plane $x/L = 2$ (2 in. upstream of the trailing edge) and in plane 1 (9 mm downstream of the trailing edge) are shown in Fig. 23. The contour plot for the downstream plane indicates sizable eddy viscosity away from the vortex core. Large eddy viscosity far from the vortex core arises in the wake because the Baldwin–Lomax turbulence model requires one to find the maximum of $|\bar{\omega}|d$ where $\bar{\omega}$ is the vorticity and d is the distance away from the center of the wake. Unfortunately, for the flow behind the trailing edge, $|\bar{\omega}|d$ oscillates and its peaks increase with increasing distance from the wake center. Contours of eddy viscosity should concentrate near the vortex core in any plane downstream from the trailing edge.

A third set of computations was attempted. The parameters for the third set are the same as for Case 2 except that the k-ϵ turbulence model was used instead of the Baldwin-Lomax turbulence model. Because computations for this case were terminated before convergence was attained, no results are presented for mean velocity components or the axial component of vorticity. However, contour plots of the eddy viscosity in the plane $x/L = 2$ (2 in. upstream of the trailing edge) and in plane 1 (9 mm downstream of the trailing edge) are shown in Fig. 24. These are to be compared with Fig. 23 to see the difference between the eddy viscosity for the Baldwin-Lomax turbulence model and the albeit unconverged k-ϵ turbulence model. In Fig. 24b, the contour plot of the eddy viscosity in plane 1 for the k-ϵ model seems reasonable; the corresponding contour plot in Fig. 23b for the Baldwin-Lomax model does not.
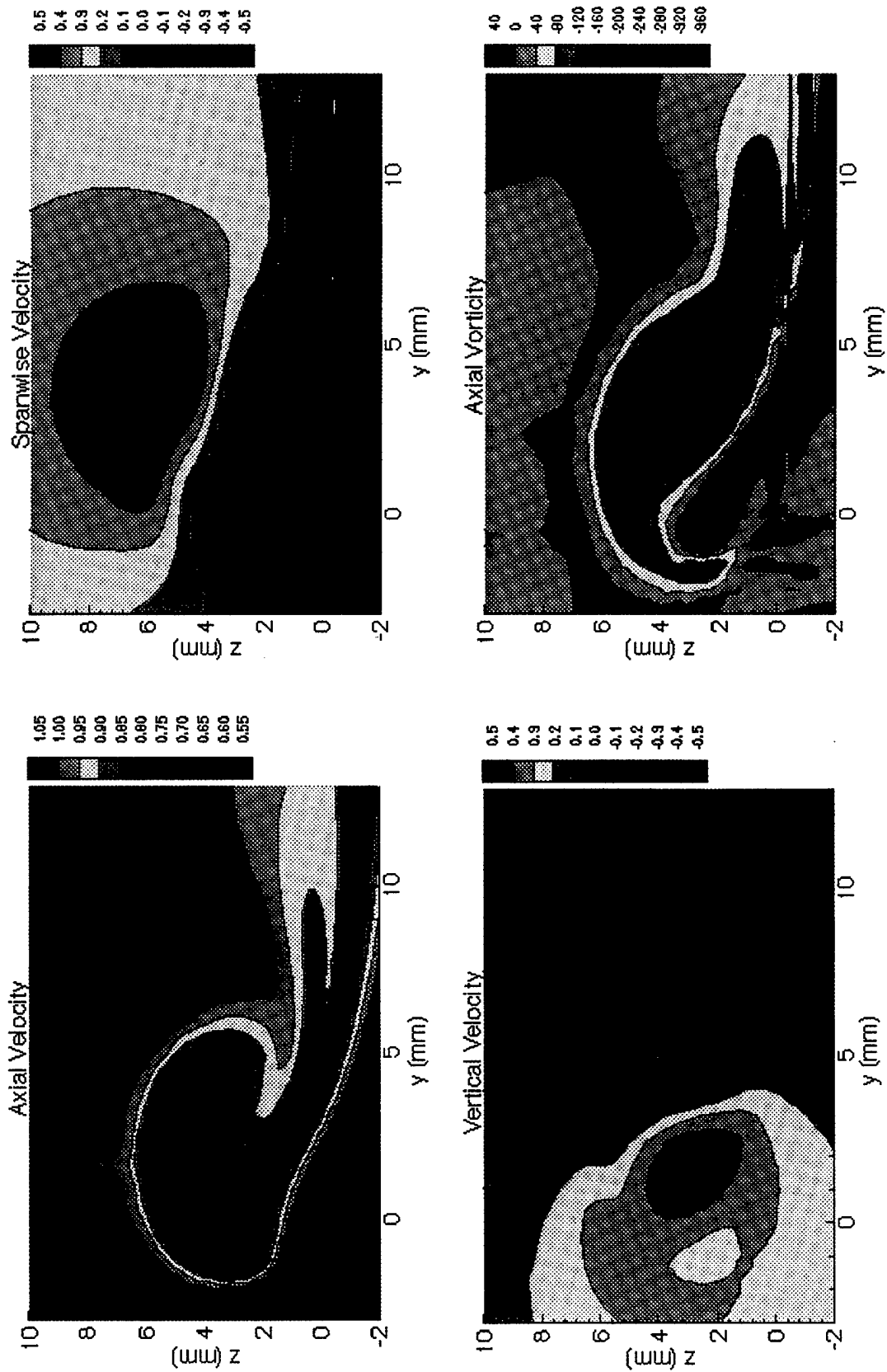
Fig. 15. Computed axial, spanwise, and vertical velocity components and axial vorticity component in plane 1 for a wholly turbulent boundary layer and $U = 24.0$ ft/s.
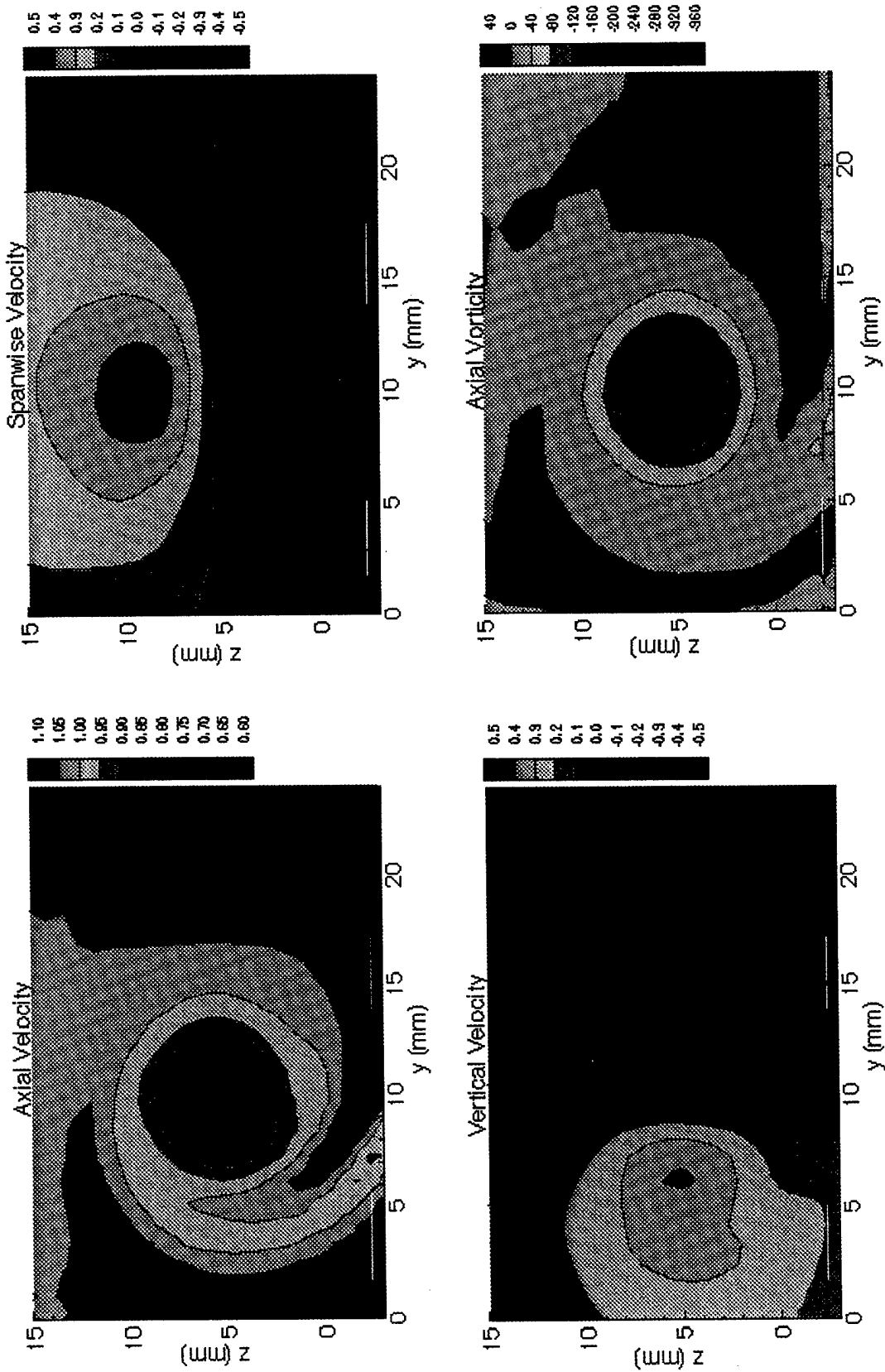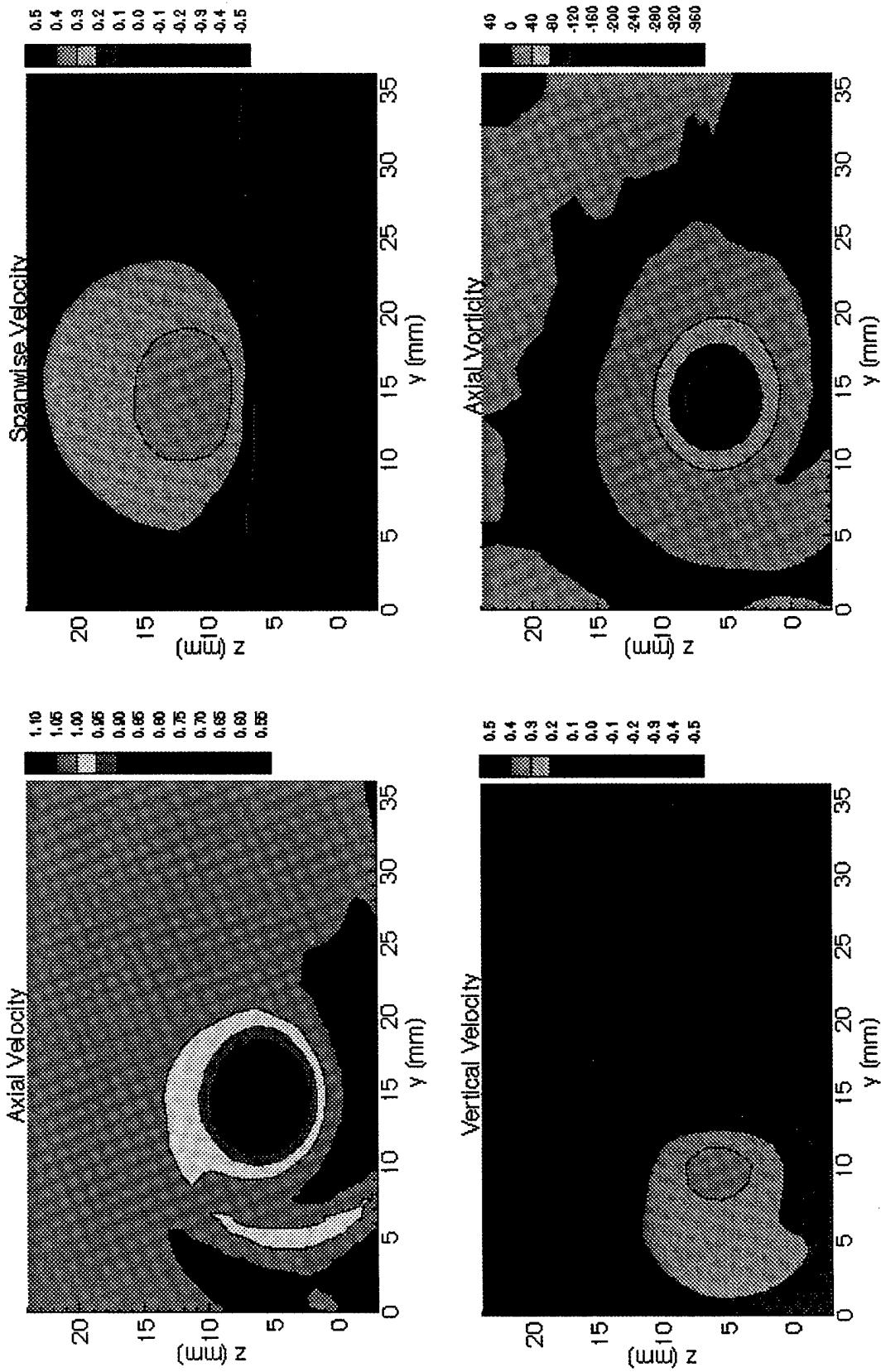
Fig. 16. Computed axial, spanwise, and vertical velocity components and axial vorticity component in plane 1A for a wholly turbulent boundary layer and $U = 24.0$ ft/s.

THIS PAGE INTENTIONALLY LEFT BLANK

Fig. 17. Computed axial, spanwise, and vertical velocity components and axial vorticity component in plane 2 for a wholly turbulent boundary layer and $U = 24.0$ ft/s.
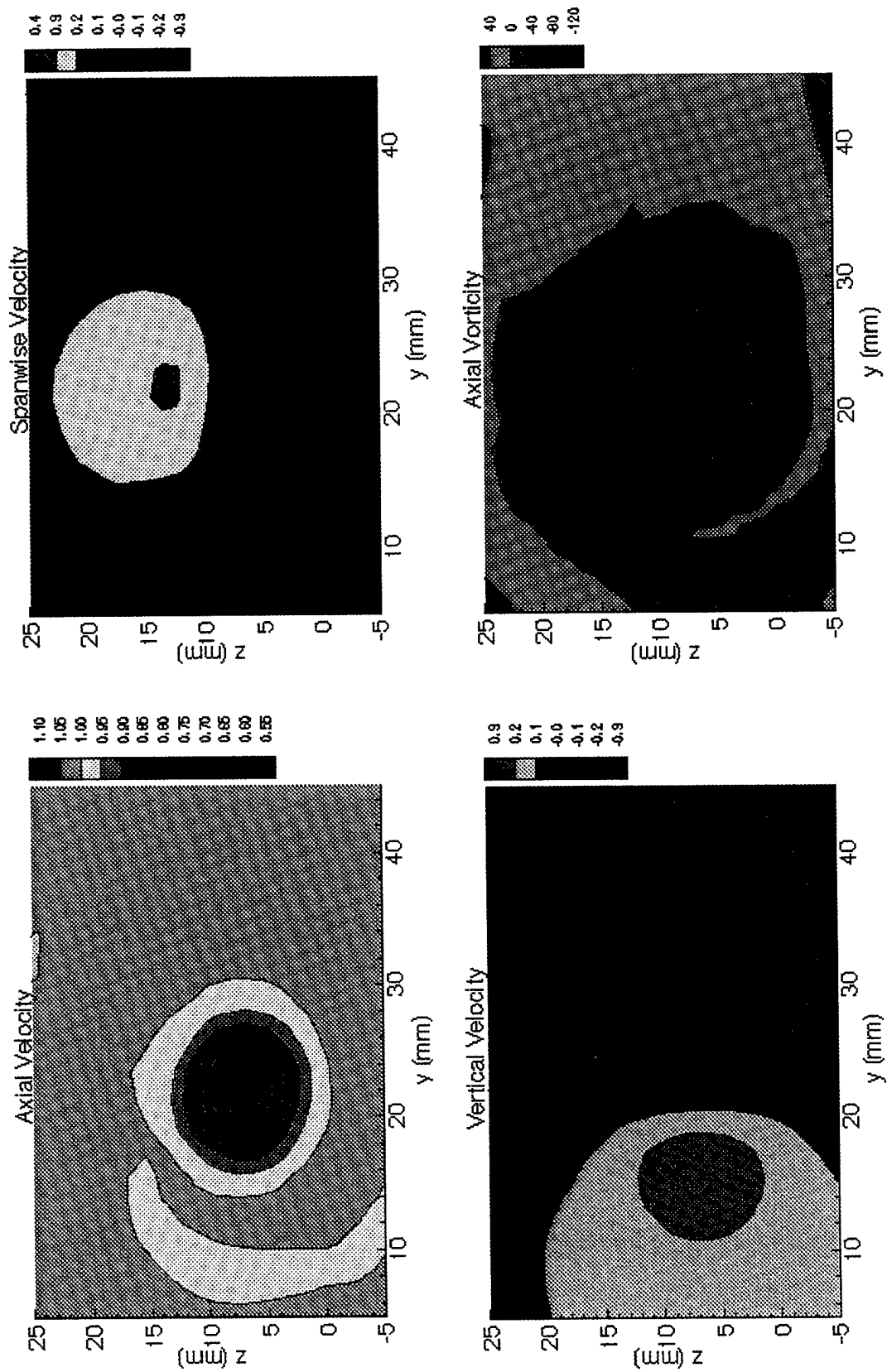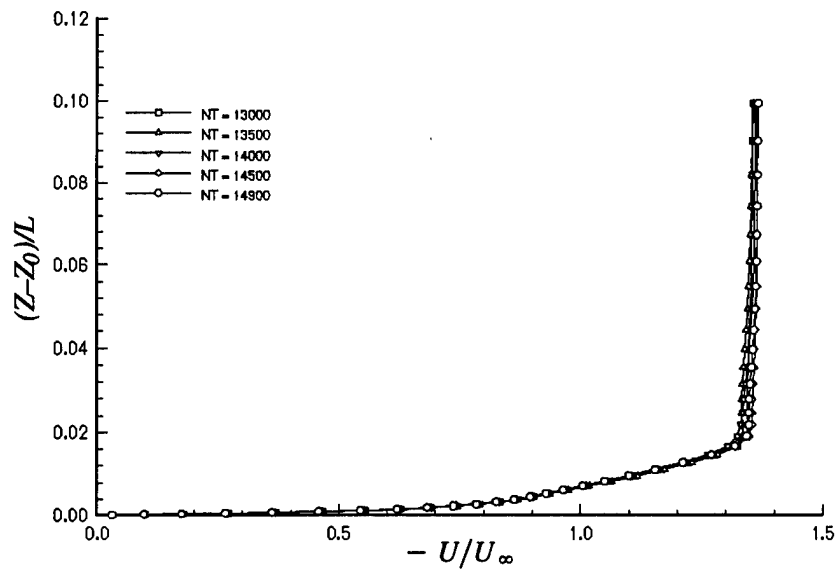
THIS PAGE INTENTIONALLY LEFT BLANK

Fig. 18. Computed axial, spanwise, and vertical velocity components and axial vorticity component in plane 3 for a wholly turbulent boundary layer and $U = 24.0$ ft/s.

37

Fig. 19. Mean streamwise velocity profile at location (a) on the wing for a wholly turbulent boundary layer and $U = 24.0$ ft/s. For location see Fig. 10.
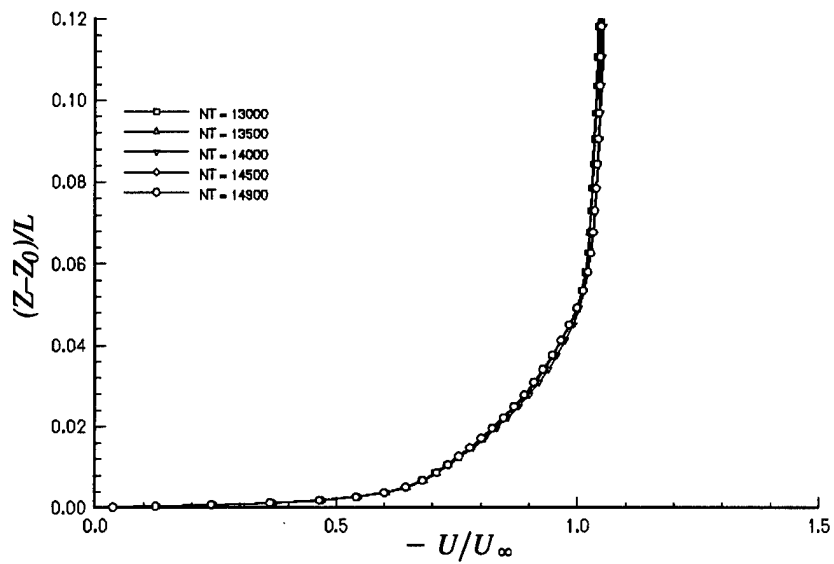
Fig. 20. Mean streamwise velocity profile at location (b) on the wing for a wholly turbulent boundary layer and $U = 24.0$ ft/s. For location see Fig. 10.
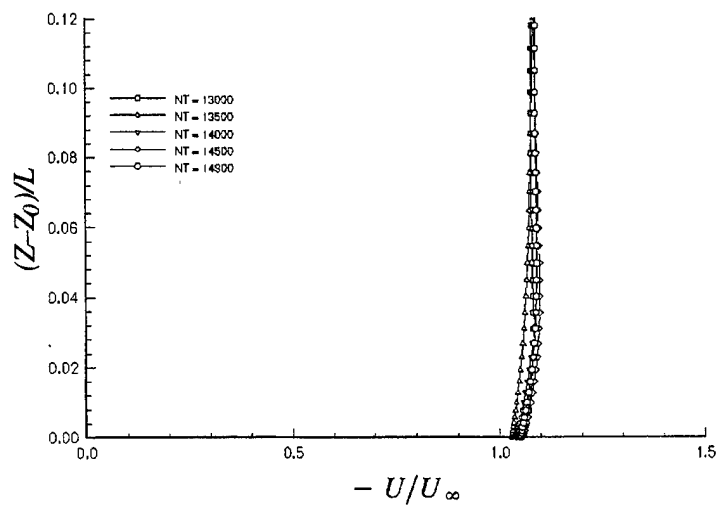
Fig. 21. Mean streamwise velocity profile at location (c) downstream of the wing for a wholly turbulent boundary layer and $U = 24.0$ ft/s. For location see Fig. 10.

Fig. 22. Mean streamwise velocity profile at location (d) downstream of the wing for a wholly turbulent boundary layer and $U = 24.0$ ft/s. For location see Fig. 10.

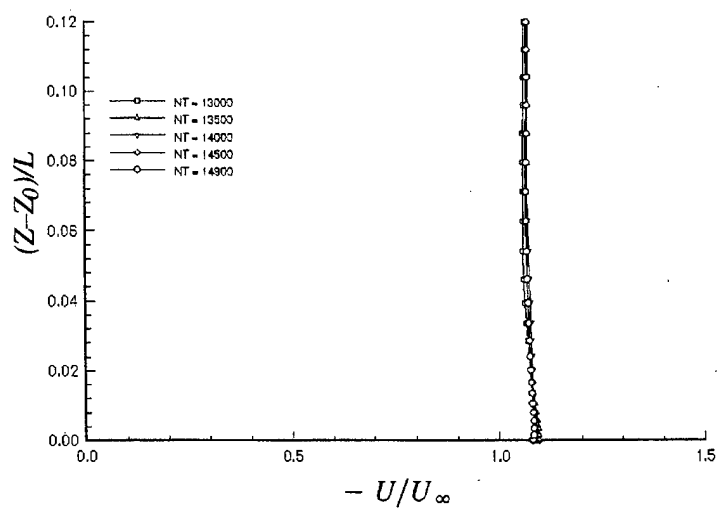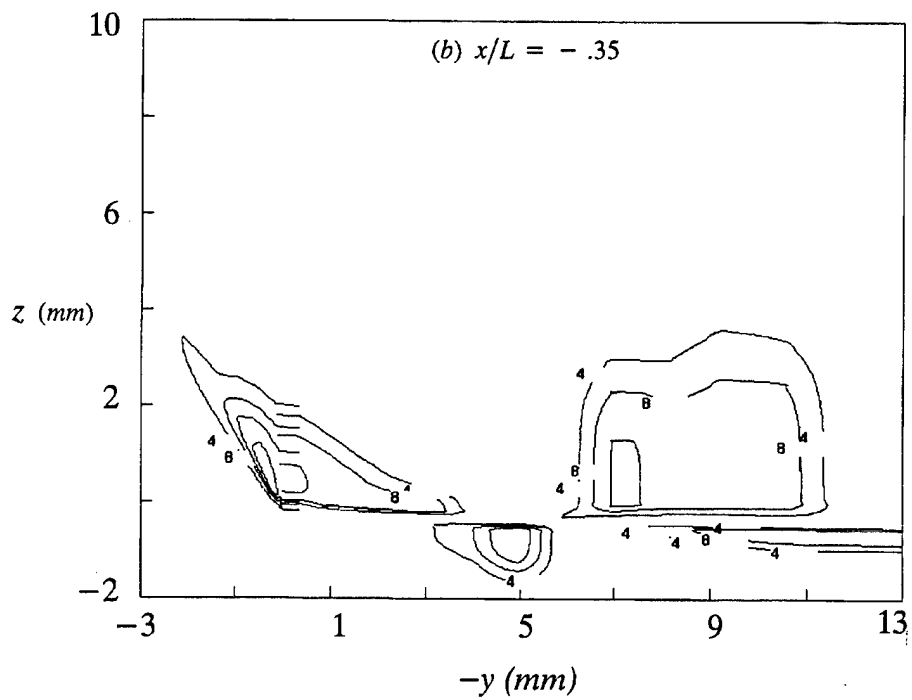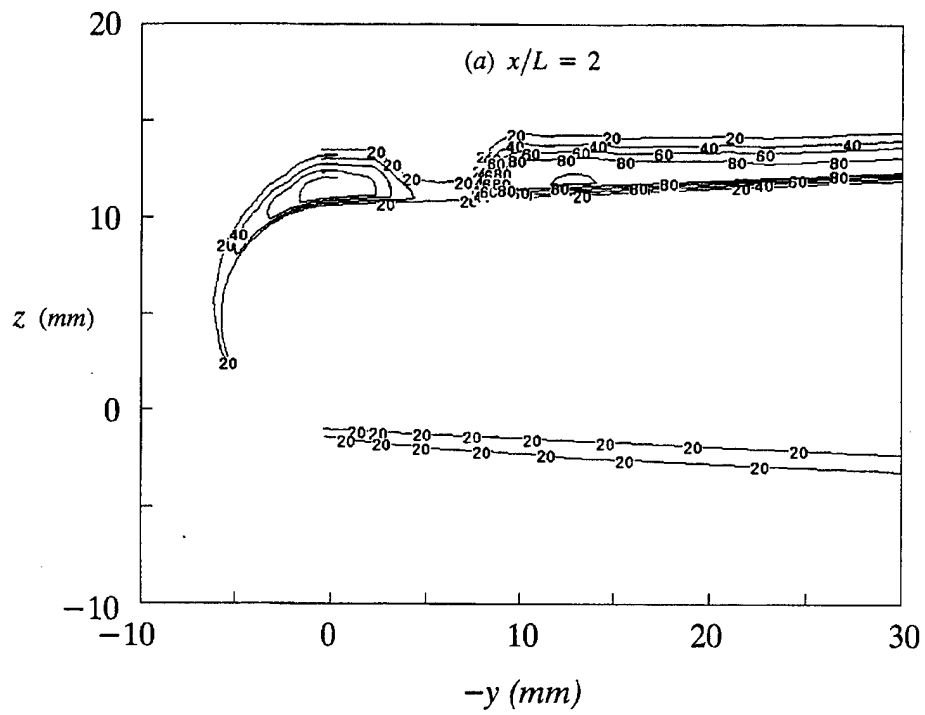**Fig. 23.** Eddy viscosity from the Baldwin-Lomax turbulence model (a) in a plane upstream of the trailing edge and (b) in a plane downstream from the trailing edge.
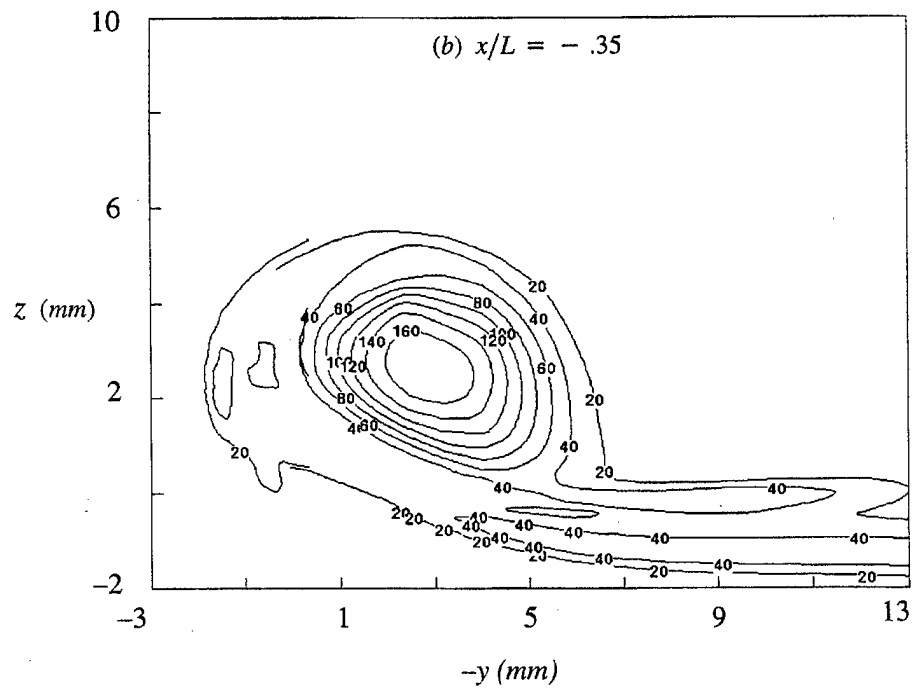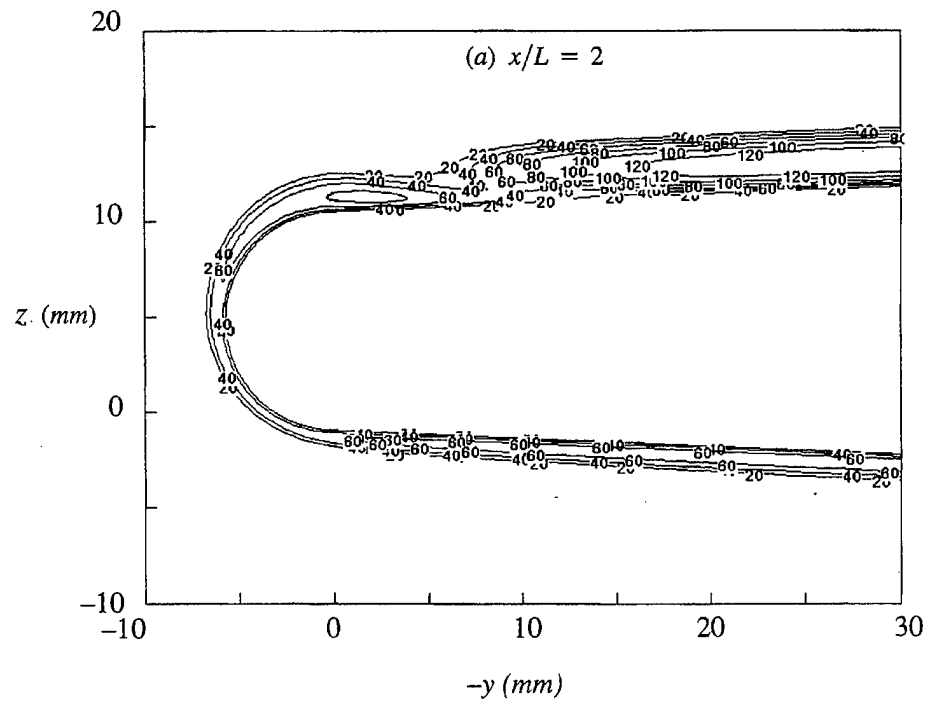
Fig. 24. Eddy viscosity from the k-ϵ turbulence model (a) in a plane upstream of the trailing edge and (b) in a plane downstream from the trailing edge.

41

THIS PAGE INTENTIONALLY LEFT BLANK

REFERENCES

1. Shamroth, S. J. and W. R. Briley, "A Viscous Flow Analysis for the Tip Vortex Generation Process," NASA CR 3184 (1979).

2. Govindan, T. R., R. Levy, and S. J. Shamroth, "Computation of the Tip Vortex Generation Process for Ship Propeller Blades," *Proc. Fourth International Conference on Numerical Ship Hydrodynamics* (1985).

3. Eça, L., J. Falcão de Campos, and M. Hoekstra, "Prediction of Incompressible Tip Vortex Flows," *Proc. Twentieth Symposium on Naval Hydrodynamics* (1994).

4. Haussling, H. J., "Computational Experiments on the Tracking of Vortices," CARDIVNSWC-TR-95/021 (1995).

5. Ramsey, W., "Control Surface Vortex Studies," MIT Department of Ocean Engineering Report 97-2 (1997).

6. Abbot, I. and A. von Doenhoff, *Theory of Wing Sections*, Dover (1959).

7. Gorski, J. J., "High Accuracy TVD Schemes for the k–ε Equations of Turbulence," AIAA Paper No. 85-1665 (1985).

8. Gorski, J. J., "A New Near-Wall Formulation for the k–ε Equations of Turbulence," AIAA Paper No. 86-0556 (1986).

9. Gorski, J. J., "TVD Solutions of the Incompressible Navier-Stokes Equations With an Implicit Multi-grid Scheme," AIAA Paper No. 88–3699, presented at the First National Fluid Dynamics Conference, Cincinnati, Ohio (24-28 Jul 1988).

10. Gorski, J. J., "Solutions of the Incompressible Navier-Stokes Equations Using an Upwind-Differenced TVD Scheme," *Lecture Notes in Physics*, Vol. 323, Eds. D. L. Dwoyer, M. Y. Hussaini, and R. G. Voigt, pp. 278-282 (1989).

11. Baldwin, B. S. and H. Lomax, "Thin Layer Approximation and Algebraic Model for Separated Turbulent Flows," *AIAA 16th Aerospace Sciences Meeting* (1978).

12. Chorin, A. J., "A Numerical Method for Solving Incompressible Viscous Flow Problems," *Journal of Computational Physics*, Vol. 2, pp. 12-26 (1967).

13. Cebici, T., K. Kaups, and J. A. Ramsey, "A General Method for Calculating Three-Dimensional Compressible Laminar and Turbulent Boundary Layer on Arbitrary Wings," NASA CR 2777 (1977).

THIS PAGE INTENTIONALLY LEFT BLANK

INITIAL DISTRIBUTION

Copies   Copies

1   ARPA   G. Jones   1   Northwest Research Associates
                                                1   D. Delisi

6   ONR
       1   333   J. Fein   2   JHU Applied Physics Laboratory
       1   333   S. Lekoudis   1   T. Schemm
       1   333   P. Purtell   1   R. Thompson
       1   333   E. Rood
       1   334   R. Vogelsong   2   U. Iowa/Mech. Eng.
       1   354   R. Kostoff   1   J. Longo
                                                1   F. Stern

1   NRL
       1   W. Sandberg   1   U. Cal. Berkeley/Nav. Arch.
                                                1   R. Yeung

4   NAVSEA
       1   03H   E. Comstock   1   U. Mich./Nav. Arch. & Mar. Eng.
       1   03HD   S. Petrie   1   R. Beck
       1   03H3   H. Chatterton
       1   03H3   C. Chen   1   Miss. State U./Aero. Eng.
                                                1   D. Whitfield

2   NSWCDD/CSS
       1   M. Hyman
       1   J. Crane

1   NUWC
       1   P. Lefebvre

1   OPNAV
       1   N87T   J. Schuster

2   Science Applications
       International Corp.
       1   G. Innis
       1   R. Korpus

1   Mass. Inst. of Tech.
       1   Dept. of Ocean Eng./J. Kerwin

1   PSU Applied Research Laboratory
       1   C. Knight

DIVISION DISTRIBUTION

Copies	Code	Name
1	0112	B. Douglas
1	0114	K.-H. Kim
1	20	R. Keane
1	26	M. Hurwitz
1	26	H. Lugt
1	261	R. VanEseltine
1	262	S. Ohring
1	262	J. Slomski
5	262	J. Telste
1	263	S. Willner
1	3023	TIC
1	50	W. Morgan
1	503	T. Huang
1	505	A. Reed
1	506	D. Walden
1	52	R. Ames
1	52	P. Chang
1	52	D. Hendrix
1	52	C. Lin
5	52	T. Ratcliffe
1	53	T. Tai
5	54	R. Coleman
1	54	C. Dai
1	54	J. Gorski
1	54	H. Haussling
1	54	Y.-T. Lee
1	54	F. Peterson
1	54	M. Wilson
1	54	C.-I. Yang
1	7051	W. Blake